JGP Journal of General Physiology

ARTICLE

Electrophysiology in nanoscale compartments

Madeleine R. Howell[1*], Rosalind J. Xu[1*], and Adam E. Cohen[1,2]

Voltage-gated ion channels play important roles in many membrane-enclosed structures, including synaptic vesicles, endosomes, mitochondria, chloroplasts, viruses, and bacteria. Here, we study how compartment size and channel gating interact to shape voltage dynamics and ion content in sub-micron structures. In small compartments, assumptions underlying conductance-based (Hodgkin–Huxley type) models of membrane voltage must be relaxed: (1) stochastic gating of individual ion channels can quickly and substantially change membrane voltage; (2) these changes can equilibrate faster than channel state dwell times; and (3) ionic currents, even though as few as two channels, can substantially alter ionic concentrations. We adapted conductance-based models to incorporate these effects, and we then simulated voltage dynamics of small vesicles as a function of vesicle radius and channel density. We identified regimes in this parameter space with qualitatively distinct dynamics. We then performed stochastic simulations to explore the role of $Na_V1.5$ in the maturation of macrophage endosomes. The stochastic model predicted dramatically different dynamics compared with a deterministic approach. Electrophysiology of nanoscale structures can be very different from larger structures, even when ion channel composition and density are preserved.

Introduction

Ion channels and pumps operate not only in large, patch-clamp–accessible cells but also in many small membrane-enclosed structures, including synaptic vesicles (Rahamimoff et al., 1988; Takamori et al., 2006), endosomes (Carrithers et al., 2007), lysosomes (Wang et al., 2017), mitochondria (Ichas et al., 1997), chloroplasts (Finazzi et al., 2015), and diverse microbes and viruses (Martinac et al., 1987; Berrier et al., 1996; Radchenko et al., 2006; Martinac et al., 2008; Sze and Tan, 2015) (Fig. 1 A). Electrochemical gradients in these compartments are integral to cell physiology: they drive ATP synthesis in mitochondria (Sorgato et al., 1987); regulate acidification and cargo processing in secretory and endocytic organelles (Takamori et al., 2006; Modi et al., 2009; Scott and Gruenberg, 2011); and contribute to pH- and voltage-dependent stages of viral entry (Pinto et al., 1992; Akole and Warner, 2019). In bacteria, voltage- and mechano-sensitive ion channels participate in the homeostasis of membrane potential, osmotic pressure, and ionic balance (Berrier et al., 1996; Payandeh and Minor, 2015). Yet, despite their ubiquity and functional importance, the electrophysiology of submicron compartments has historically been difficult to interrogate because of their small size, intracellular location, and (in microbes) the presence of a cell wall (Cohen and Venkatachalam, 2014).

This experimental barrier is now largely breached. Genetically encoded voltage indicators (Adam et al., 2019; Kannan et al., 2022; Abdelfattah et al., 2023; Lu et al., 2023; Tian et al., 2023; Hao et al., 2024) and small-molecule dyes (Miller et al., 2012; Yan et al., 2023; Navarro et al., 2024; Antic et al., 2025) enable *in situ* voltage measurements in small and/or intracellular membranes (Cohen and Venkatachalam, 2014; Sepehri Rad et al., 2018), with targeted implementations in mitochondria (Crowley et al., 2016; Kowaltowski and Abdulkader, 2024), dendritic spines (Cornejo et al., 2021), distal astrocytic processes (Armbruster et al., 2022), lysosomes (Modi et al., 2009; Saminathan et al., 2021), and bacteria (Kralj et al., 2011; Benarroch and Asally, 2020). Complementing protein and dye indicators, DNA-based probes have directly reported organelle electrical and ionic state variables in live cells: an organelle-targeted "voltmeter" reported absolute membrane potentials across multiple organelle classes (Saminathan et al., 2021); single-organelle Na^+ mapping revealed pronounced heterogeneity and maturation-dependent shifts in lumenal sodium (Zou et al., 2024); and an organelle-localized reporter indicated that voltage-gated K^+ channels (K_V's) canonically associated with the plasma membrane can be functionally active on trafficking organelles, with measurable consequences for lumenal K^+ (Anees et al., 2024).

Together, these experiments raise mechanistic questions that are difficult to answer with classical electrophysiology models: how are organelle voltages and Na^+/K^+ gradients established and maintained when copy numbers of channels and transporters are small (Sabatini and Svoboda, 2000; Mutch et al., 2011; McVeigh et al., 2025)? When organelle-to-organelle variability

[1]Department of Chemistry and Chemical Biology, Harvard University, Cambridge, MA, USA; [2]Department of Physics, Harvard University, Cambridge, MA, USA.

*M.R. Howell and R.J. Xu contributed equally to this paper. Correspondence to Adam E. Cohen: cohen@chemistry.harvard.edu.

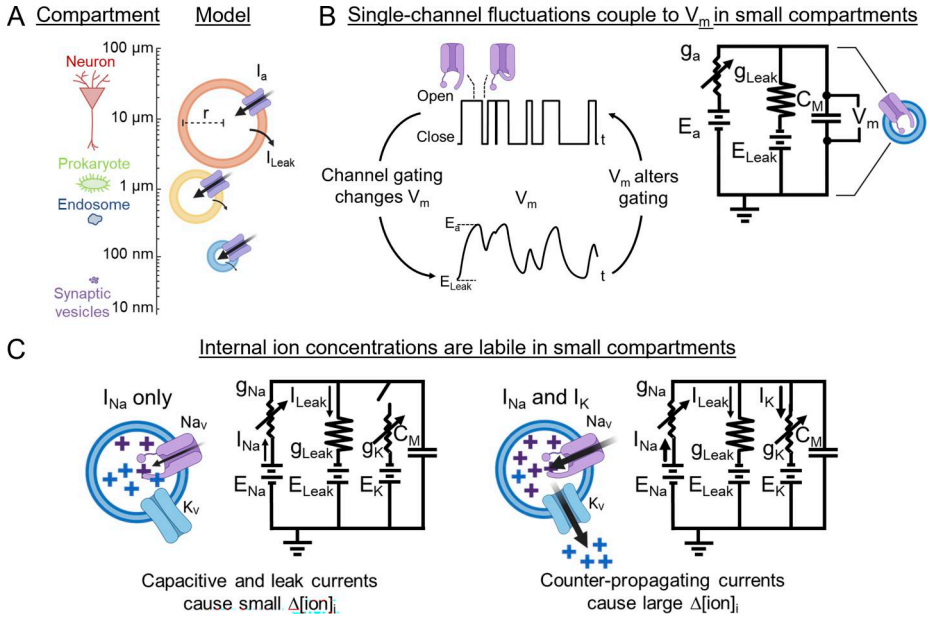

Figure 1. **Small compartments have distinctive electrophysiology. (A)** Bioelectrical dynamics occur over a wide range of spatial scales. Excitable compartments (left) and model vesicles with simplified geometry (right). **(B)** In a small compartment, stochastic gating of a single channel changes V_m, which then affects channel gating. Changes in V_m alter the duration of individual channel open events and introduce an effective gating "memory" into the dynamics, despite the use of a Markovian channel model. In the circuit diagram, the size of the leak resistor indicates $g_{Leak} \ll g_a$. **(C)** Coincident activation of channels with different reversal potentials can drive spontaneous depletion of ionic concentration gradients. Upon Na_V opening, I_{Na} charges the membrane capacitance and then maintains steady-state flow out via I_{Leak} (left panel). For realistic parameters, the capacitive charging current has little effect on internal Na^+ concentration. When Na_V and K_V opening coincide, inward I_{Na} is balanced by outward I_K until E_{Na} and E_K are equal (right panel). This current drives large changes to internal ion concentrations. Abbreviations: g_a, single-channel conductance of an arbitrary channel; g_{Na}, Na_V single-channel conductance; g_{Leak}, leak conductance; g_K, K_V single-channel conductance; E_a, reversal potential of an arbitrary channel; E_{Na}, Na^+ reversal potential; E_{Leak}, leak reversal potential; E_K, K^+ reversal potential; I_{Na}, Na_V current; I_{Leak}, leak current; I_K, K_V current; C_M, membrane capacitance; V_m, membrane potential. Created in BioRender. Howell, M. (2025) https://BioRender.com/nm7zk94.

is large (Zou et al., 2024), does this reflect deterministic maturation-dependent shifts, stochastic variations in channel number, or rare but consequential stochastic gating events? And how do transient channel openings during trafficking reshape lumenal ion composition, potentially modulating downstream processes such as acidification, cargo sorting, and maturation (Modi et al., 2009; Scott and Gruenberg, 2011)?

Answering these questions presents a challenge for the standard theoretical framework for membrane voltage—the Hodgkin–Huxley (HH) family of conductance-based models—which rests on approximations appropriate for large membranes with many copies of each ion channel type. First, HH-type descriptions are mean-field: conductances represent ensemble averages over many channels, and fluctuations are commonly treated as small perturbations around the mean. In the regime of finite-but-large channel number N, channel noise is often well approximated by a Gaussian perturbation to conductance (or gating variables), yielding Langevin/Fokker–Planck descriptions in which voltage performs a diffusion-like biased random walk about a stable fixed point and spiking can be described as a Kramers escape process (Skaugen and Walløe, 1979; Chow and White, 1996; White et al., 1998; White et al., 2000; Mino et al., 2002; Schmid et al., 2003; Faisal et al., 2005; Goldwyn and Shea-Brown, 2011). A substantial literature has explored how membrane area and morphology filter or amplify this conductance noise and how it impacts spike timing and reliability (Johansson and Arhem, 1994; Faisal et al., 2005; Zeng et al., 2007; Cannon et al., 2010). These approaches have been powerful precisely because individual channel events contribute only weakly to V_m, and because averaging over many channels smooths the dynamics.

Sub-micron compartments can instead inhabit a qualitatively different regime in which voltage dynamics are dominated by discrete single-channel gating events, not by Gaussian fluctuations around a mean conductance. Two scaling relations drive this transition. (1) Membrane leak conductance scales with membrane area, so the same single-channel current produces a larger steady-state ΔV_m in a smaller compartment; in sufficiently small structures, opening of a single channel can drive V_m close to that channel's reversal potential. (2) The membrane charging time in small structures can become fast compared with the characteristic channel state-transition times, so channels "feel" their own impact on V_m during an opening event. This self-action breaks the separation between channel kinetics and voltage dynamics that underlies diffusion approximations: instead of nearly continuous, Gaussian-like voltage noise, the system exhibits jump-like trajectories with history-dependent effective kinetics (Fig. 1 B). In this regime, it is no longer sufficient to treat stochasticity as a small, additive perturbation to HH dynamics.

A second HH assumption also can break down in small compartments: that (except for Ca^{2+}) ionic concentrations are

effectively constant on the timescale of electrical activity. Extensions of conductance-based models to include dynamic ion concentrations and pumps have been developed for neurons and cardiac tissue (DiFrancesco and Noble, 1997; Hübel and Dahlem, 2014), but typically in parameter regimes where concentration changes are slow compared with individual spikes. In contrast, the same small volumes that amplify voltage responses also amplify concentration changes driven by ionic fluxes; moreover, coincident opening of channels with distinct reversal potentials can produce large counter-propagating ionic currents even when net membrane current is small, rapidly dissipating gradients in ways not captured by fixed-reversal-potential models (Fig. 1 C). The relevance of this issue is underscored by emerging measurements showing that organellar ionic contents can be variable and responsive to channel activity (Anees et al., 2024; Zou et al., 2024). Thus, a theory aimed at interpreting voltage and ion measurements in small compartments must simultaneously confront (1) discrete stochastic gating that directly controls V_m, (2) feedback from V_m onto channel gating on the timescale of single gating events, and (3) time-dependent driving forces arising from labile ionic gradients.

Here, we adapt conductance-based electrophysiology to explicitly incorporate these small-compartment effects. We treat channel gating as discrete stochastic jump processes (Markov state models) coupled self-consistently to membrane voltage, and we update ionic concentrations (and hence reversal potentials) as currents flow in nanoscale volumes. We use this framework to map regimes of qualitatively distinct dynamics as a function of vesicle size and channel density, to identify when deterministic HH-like descriptions approximate stochastic dynamics and when they fail, and to predict new behaviors—such as voltage "memory" and gradient-depletion–mediated refractoriness—that emerge when single-channel events dominate. Finally, motivated by experimental reports of voltage-gated Na^+ channel (Na_V)1.5 in macrophage endosomes and its proposed role in acidification (Carrithers et al., 2007), we apply the stochastic, concentration-aware framework to endosome maturation, illustrating how rare channel openings can produce outsized physiological consequences in a small compartment. While we primarily analyze the roles of Na_V and K_V, the methodology is not limited to the canonical HH channels, but can apply to the many organelle-specific channels and transporters (Xu et al., 2015). Together, these results provide a quantitative framework for emerging measurements of voltage and ionic composition in organelles, microbes, and other small compartments, and they suggest experimentally testable signatures of the single-channel-dominated regime.

Materials and methods

All simulations were performed in MATLAB.

Single-channel vesicle model

We examine the interaction between stochastic channel gating and membrane voltage (V_m) using a single 14 pS conductance Na_V in the membrane of a spherical vesicle. The vesicle also contains a nonspecific and deterministic leak conductance proportional to vesicle area (A_m) with $g_{Leak} = 1\frac{pS}{\mu m^2} \times A_m$ and the leak reversal potentials (E_{Leak}) given below. Simulations of vesicle V_m are initialized at $V_m = E_{Leak}$. Because unidirectional single-channel currents do not substantially alter internal electrolyte concentrations, in these simulations Na^+ and leak reversal potentials are held fixed. The Markovian model of stochastic Na_V gating is described below (Markovian dynamics for voltage-gated ion channels) and in Note S1 in the Supplemental text at the end of the PDF. To examine the role of window currents on channel behavior, we modify Na_V kinetics to yield a model with substantial window current (Na_V^+) as well as negligible window current (Na_V^-). These modifications are described in Note S1 in the Supplemental text.

We simulate (1) V_m in response to a single channel opening (Fig. 2 A) with $E_{Leak} = -93$ mV; (2) time-to-close of a channel initialized in the open state (Fig. 2 C) with $E_{Leak} = -25$ mV, and (3) spontaneous trajectories of channel gating and V_m using either the default Na_V model (Fig. 2 B) with $E_{Leak} = -25$ mV, or the modified window current models (Fig. 2 G) with $E_{Leak} = -60$ mV. The depolarized E_{Leak} of -25 mV in (2) and (3) was chosen such that V_m does not transit the window current regime, to isolate the effect of depolarization on channel kinetics and memory. E_{Leak} of -60 mV in (3) was chosen such that channel activation forced V_m to transit the window regime.

Annotated code for simulating the dynamics in Fig. 2, B, C, and G, is available at: https://github.com/adamcohenlab/howell2025small-scale-ephys/tree/main/code-single_NaV_vesicles.

HH-type vesicle model

We examine the ensemble effects of stochastic and counter-propagating currents in vesicles with HH-like Na_V, $*K_V$, and leak conductances. While the original HH model does not explicitly consider intracellular ion concentrations, it can be extended to an ion-specific form (Hodgkin and Huxley, 1952; Chay and Keizer, 1983; Sherman et al., 1988; Sherman and Rinzel, 1991; Barreto and Cressman, 2011; Krishnan and Bazhenov, 2011; Hübel and Dahlem, 2014; Hübel et al., 2014). Following the conventions of Hübel et al., the ion concentrations and reversal potentials are updated at each time step, a Na^+/K^+-ATPase model is added to restore the Na^+/K^+ balance, and the nonspecific leak current is rendered ion-specific (Hübel and Dahlem, 2014; Hübel et al., 2014). Na_V and K_V are modeled as discrete and stochastic with Markovian dynamics (described in Markovian dynamics for voltage-gated ion channels). All other conductances are modeled as continuous and deterministic. We assume similar mobilities for Na^+ and K^+ ions, so the contribution of each ion to the injected current is proportional to its mole fraction in the extravesicular solution. The formulation is

$$\frac{dV_m}{dt} = -\frac{1}{C_M}\left(I_{Na^+} + I_{K^+} + I_{Cl^-}\right) \quad \text{M1}$$

$$I_{Na^+} = \left(g_{Na_V} N_{open,Na_V} + g_{Na^+,leak}\right)\left(V_m - E_{Na^+}\right) - I_{inj}\frac{[Na^+]_o}{[Na^+]_o + [K^+]_o} + 3I_{pump} \quad \text{M2}$$

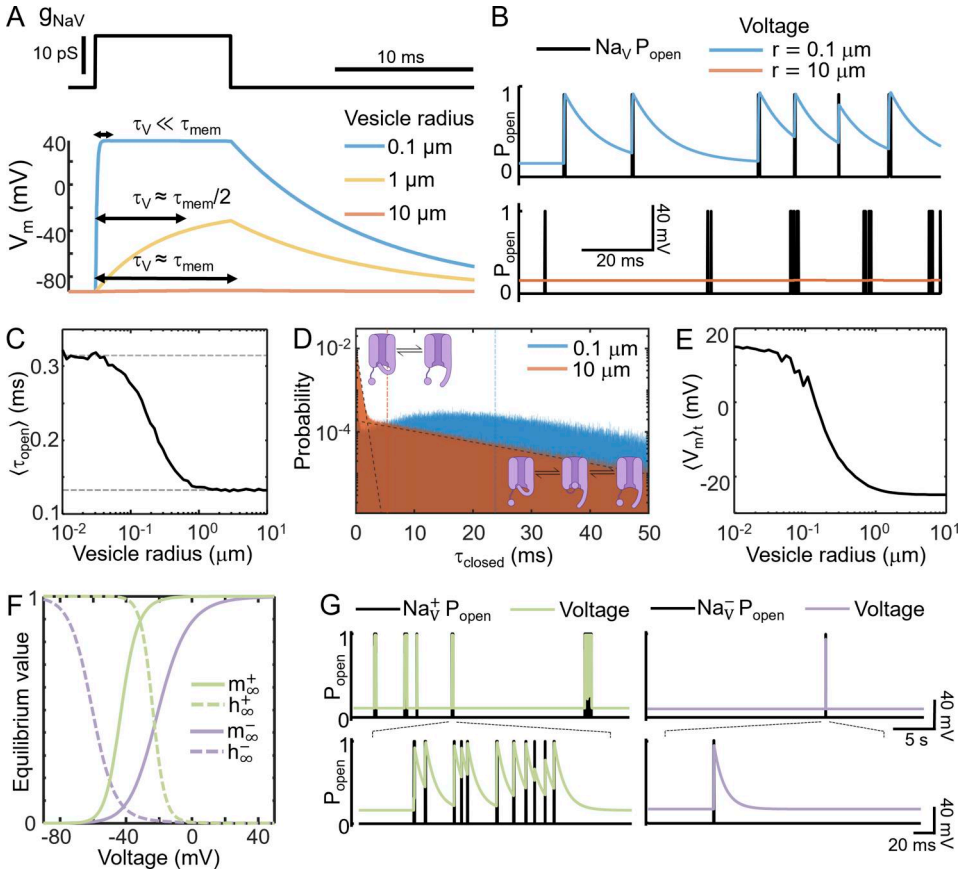

Figure 2. **Reciprocal interactions between single-channel gating and V_m fluctuations in small compartments. (A)** Simulated V_m in response to a single Na_V opening in vesicles of varying size. τ_V is the time constant of the voltage response when the channel is open; τ_{mem} is the intrinsic membrane time constant (when the channel is closed). **(B)** Spontaneous Na_V gating (black) and V_m for r = 10 μm (orange) and r = 0.1 μm (blue). Leak reversal potential, E_{Leak} = − 25 mV. **(C)** Mean Na_V open-state dwell time as a function of vesicle radius; average of $n = 10^4$ simulations of a Na_V initialized in the open state with V_m (t = 0) = E_{Leak}. Dashed lines show open-state dwell time when V_m is clamped at $V_m = E_{Leak}$ (bottom) and $V_m = E_{Na}$ (top). **(D)** Closed-state dwell time histograms for voltage trajectories in vesicles with r = 10 μm and 0.1 μm, calculated as in B; simulations 5,000 s. Black dashed lines indicate linear fits to the fast τ^{short}_{closed} = 0.47 ± 0.01 ms (95% confidence) and slow τ^{long}_{closed} = 17 ± 0.07 ms (95% confidence) closed state dwell times for the r = 10 μm vesicle. Orange and blue vertical lines indicate mean τ_{closed} for r = 10 μm (5.4 ± 12 ms) and 0.1 μm (24 ± 19 ms) vesicles (mean ± SD). **(E)** Time-average membrane voltage during spontaneous single-channel gating trajectories as in B. Each data point is an average of five 50-s-long simulations. **(F)** Steady-state activation (solid trace) and inactivation (dashed) curves for a Na_V model with a large window current (Na_V^+, light green) and a Na_V model with a small window current (Na_V^-, light purple). **(G)** Spontaneous Na_V gating (black) and V_m for the Na_V^+ model (left, light green) and the Na_V^- model (right, light purple) in F, for r = 0.1 μm vesicles at E_{Leak} = − 60 mV. The Na_V^+ model voltage chatters between epochs of high-frequency oscillation and quiescent epochs. Created in BioRender. Howell, M. (2025) https://BioRender.com/nm7zk94.

$$I_{K^+} = \left(g_{K_V} \cdot N_{open,K_V} + g_{K^+,leak}\right)\left(V_m - E_{K^+}\right) - I_{inj}\frac{[K^+]_o}{[Na^+]_o + [K^+]_o} - 2I_{pump} \quad \text{M3}$$

$$I_{Cl^-} = g_{Cl^-,leak}\left(V - E_{Cl^-}\right) \quad \text{M4}$$

$$I_{pump} = I_{pump,max}\left(1 + e^{\frac{25 - [Na^+]_i}{3}}\right)^{-1}\left(1 + e^{5.5 - [K^+]_o}\right)^{-1} \quad \text{M5}$$

Here, V_m is the membrane potential which is defined relative to the cytosol, i.e., $V_m = V_{lumen} - V_{cytosol}$, C_M is the membrane capacitance, E_{ion} is the reversal potential; I_{ion} is the ionic current (flow from lumen to cytosol is defined as positive), I_{inj} is the injection current, I_{pump} is the Na^+/K^+-ATPase current; g_{ion_V} is the conductance of a single voltage-gated channel, $N_{open,\,ion_V}$ is the number of open channels, $g_{ion,leak}$ is the leakage conductance, $[ion]_i$ is the internal ion concentration, and $[ion]_o$ is the external concentration. There are differing conventions on the sign for voltage and current in intracellular membranes (Bertl et al., 1992; Saminathan et al., 2021). For consistency across discussions of isolated vesicles and intracellular vesicles, we use the convention of Saminathan et al. (2021), $V_m = V_{lumen} - V_{cytosol}$. In intracellular vesicles, ion channels are typically oriented with the extracellular domains facing the lumen; as a result, gating voltages have the opposite sign to the usual values reported from measurements on plasma membranes.

All vesicles are modeled as spheres. The electrophysiological parameters and initial conditions of the HH-like vesicle model are in Table S1 and Note S1 in the Supplemental text.

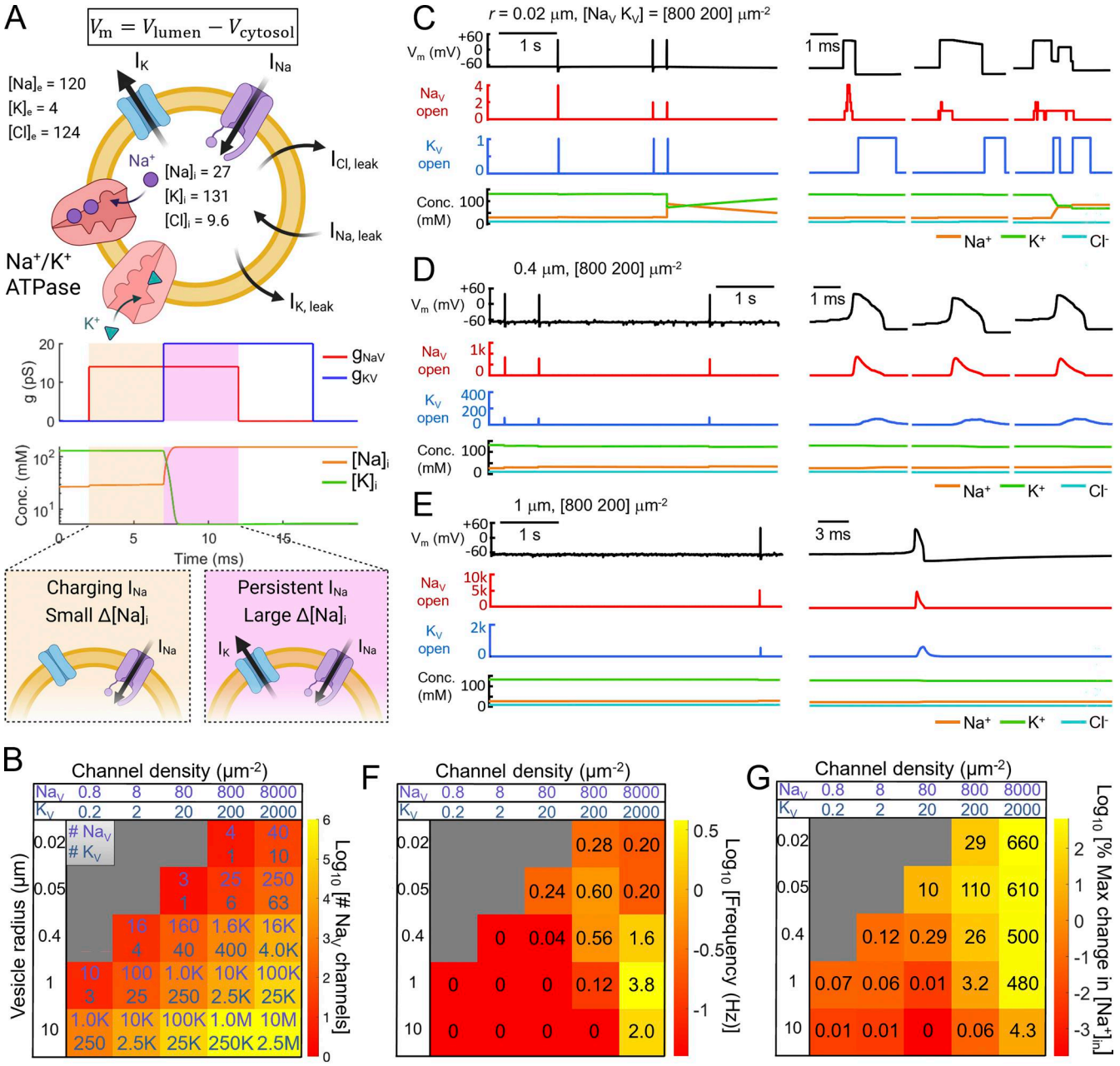

Figure 3. **Spontaneous voltage dynamics in small compartments.** Voltage and ion concentration dynamics were simulated in vesicles with different sizes and channel densities. **(A)** Top: Model vesicle with HH-type conductances and Na^+/K^+-ATPase. All concentrations in mM. Beige panels: Activation of an individual Na_V does not appreciably change internal $[Na^+]$. Pink panels: Concurrent Na_V and K_V activation depletes $[Na^+]$ and $[K^+]$ concentration gradients until the Na^+ and K^+ reversal potentials become equal. Plots are for an r = 0.02 µm vesicle. **(B)** Range of vesicle sizes and channel densities investigated. Gray regions correspond to size and density combinations with < 1 K_V per vesicle. **(C)** Left: 5-s simulation of a vesicle with r = 0.02 µm and [Na_V, K_V] = [800, 200] µm^2, corresponding to 4 Na_V's and 1 K_V. Right: Close-up of the three spontaneous events. In the third event, Na_V and K_V activation overlapped in time, leading to partial dissipation of the ionic gradients. **(D)** Left: 5-s simulation of a vesicle with r = 0.4 µm and [Na_V, K_V] = [800, 200] µm^2, corresponding to 1,600 Na_V's and 400 K_V's. Overlapping spontaneous Na_V activations were sufficient to trigger well-defined spikes. Changes in internal ionic composition were small, on account of the larger vesicle size compared with C. **(E)** 5-s simulation of a vesicle with r = 1 µm and [Na_V, K_V] = [800, 200] µm^2, corresponding to 10,000 Na_V and 2,500 K_V's. Due to the larger vesicle size, the influence of each gating event diminished compared with the vesicle in D. Channel noise led to small fluctuations in baseline voltage, which occasionally triggered spontaneous spikes. **(F)** Color map of average spontaneous spiking frequency as a function of vesicle radius and channel density. **(G)** Color map of the average percent amplitude of internal $[Na^+]$ concentration changes as a function of vesicle radius and channel density. These fluctuations were driven by overlapping Na_V and K_V currents. Data in F and G are the mean of five, 5-s simulations, excluding the r = 10 µm and [Na_V, K_V] = [8,000, 2,000] µm^2 vesicle, which was simulated for 500 ms due to computational constraints. Created in BioRender. Howell, M. (2025) https://BioRender.com/nm7zk94.

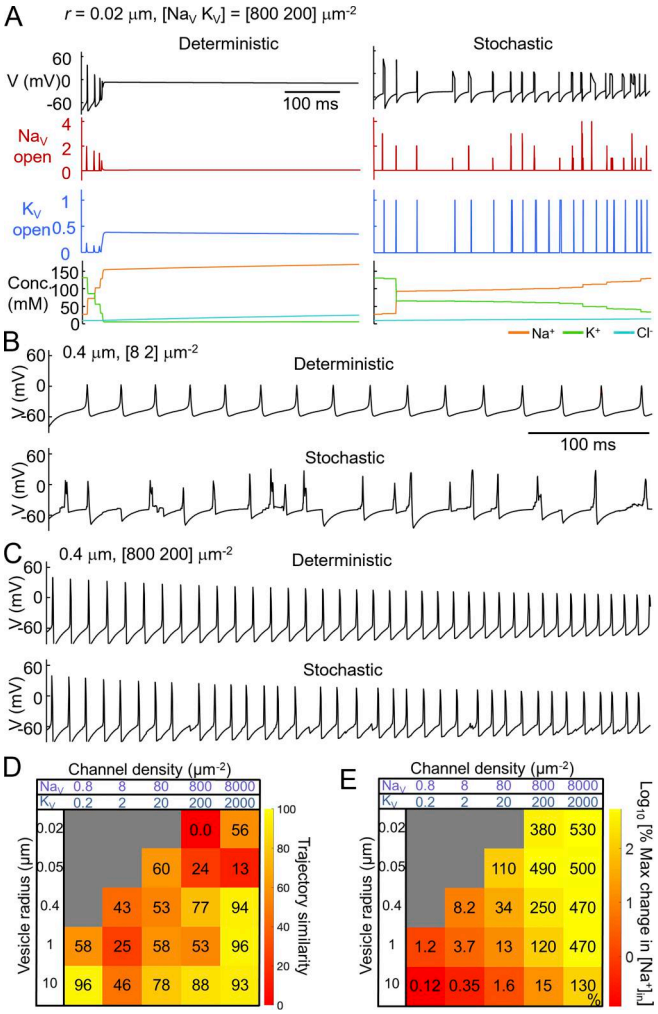

Figure 4. **Driven voltage dynamics in small compartments.** Simulations were performed as in Fig. 3, with the addition of a constant inward current density (see Materials and methods). **(A)** At the smallest vesicle size, the deterministic simulation (left) quickly entered depolarization block. In the stochastic simulations (right), fluctuations in channel gating restored the voltage from depolarization block, leading to sustained, but erratic, spiking. **(B)** In an r = 0.4 μm vesicle with low channel density, the evoked spikes were variable in waveform due to stochastic variations in the number and timing of channel opening. **(C)** In an r = 0.4 μm vesicle with higher channel density, stochastic channel fluctuations caused spike timing to be more variable than in deterministic simulations. **(D)** Color map of the similarity between stochastic and deterministic responses to current injection, as measured by cross-correlation (see Materials and methods). In the gray region, there is < 1 K_V. **(E)** Color map of the percent amplitude of internal $[Na^+]$ concentration changes as a function of vesicle radius and channel density. Data in D and E are from one, 5-s simulation, excluding the r = 10 μm and $[Na_V, K_V]$ = [8,000, 2,000] μm² vesicle, which was simulated for 500 ms.

Annotated code to simulate the dynamics in Figs. 3 and 4 is available at: https://github.com/adamcohenlab/howell2025small-scale-ephys/tree/main/code-HH_neuron_vesicles.

To compare dynamics between deterministic and stochastic simulations, we used the autocorrelation of the spike train. We chose this measure because it was not sensitive to the precise spike timing. Our measure of similarity plotted in Fig. 4 D was: $\left(1-\frac{\text{rmsd}}{\text{rmsd}_{\max}}\right)\times 100\%$, where rmsd is the root-mean-square deviation between the autocorrelation traces, and $\text{rmsd}_{\max}$ is the maximum rmsd seen across all vesicle sizes and channel densities.

Endosome model

We study the combined effects of stochastic channel dynamics and ion concentration changes in intracellular endosomes. Carrithers et al. reported $Na_V1.5$ channels in macrophage late endosomes and suggested a role in endosome acidification, a part of endosome maturation (Carrithers et al., 2007). We investigate the role of $Na_V1.5$ conductance in acidification, although a nonconducting role for the channel has not been ruled out. The minimal endosome model includes $Na_V1.5$, vacuolar-type H^+ ATPase (v-ATPase), and H^+/Cl^- exchange transporter 7 (ClC-7) (Grabe et al., 2000; Ishida et al., 2013; Balbi et al., 2017). The $Na_V1.5$ channels are inserted in an inverted orientation relative to the cell membrane; i.e., the intracellular domain (C-terminus) is facing the outside of the endosome. For ClC-7, a 2:1 Cl^-/H^+ coupling ratio is assumed. The formulation is

$$\frac{dV_m}{dt} = -\frac{1}{C_m}\left(I_{Na^+} + I_{Cl^-} + I_{H^+}\right) \quad \text{M6}$$

$$I_{Na^+} = g_{Na_V1.5}\cdot N_{open,Na_V1.5}\cdot\left(V_m - E_{Na^+}\right) \quad \text{M7}$$

$$I_{Cl^-} = N_{ClC-7}\cdot\left(2\cdot I_{ClC-7}\right) \quad \text{M8}$$

$$I_{H^+} = N_{ClC-7}\cdot I_{ClC-7} - N_{v-ATPase}\cdot I_{v-ATPase} \quad \text{M9}$$

$$I_{ClC-7} = F\left(V_m, [Cl^-]_i, [Cl^-]_e, [H^+]_i, [H^+]_e\right) \quad \text{M10}$$

$$I_{v-ATPase} = G\left(V_m, [H^+]_i, [H^+]_e\right) \quad \text{M11}$$

In which I_{ClC-7} is the net current through a single ClC-7 channel, $I_{v-ATPase}$ is the single-transporter v-ATPase current; the formulations for F, G (Eqs. M10 and M11) come from literature (Grabe et al., 2000; Ishida et al., 2013); $N_{channel}$ is the number of channels. The electrophysiological parameters and initial conditions of the endosome model are in Table S2.

Annotated code to simulate the dynamics in Fig. 5, B and C, is available at: https://github.com/adamcohenlab/howell2025small-scale-ephys/tree/main/code-endosome.

Markovian dynamics for voltage-gated ion channels

To facilitate the direct comparison between stochastic and deterministic channel dynamics, Markovian state transition models are used for voltage-gated ion channels in all simulations. The Markovian models for HH-type Na_V and K_V, as well as the $Na_V1.5$ channel, come from the literature (Gillespie, 1977; Skaugen and Walløe, 1979; Chow and White, 1996; Schmandt and Galán, 2012; Balbi et al., 2017). The deterministic channel dynamics formulation is:

$$\frac{dN_k}{dt} = \sum_i \alpha_{i\to k} N_i - \sum_i \alpha_{k\to i} N_k \quad \text{M12}$$

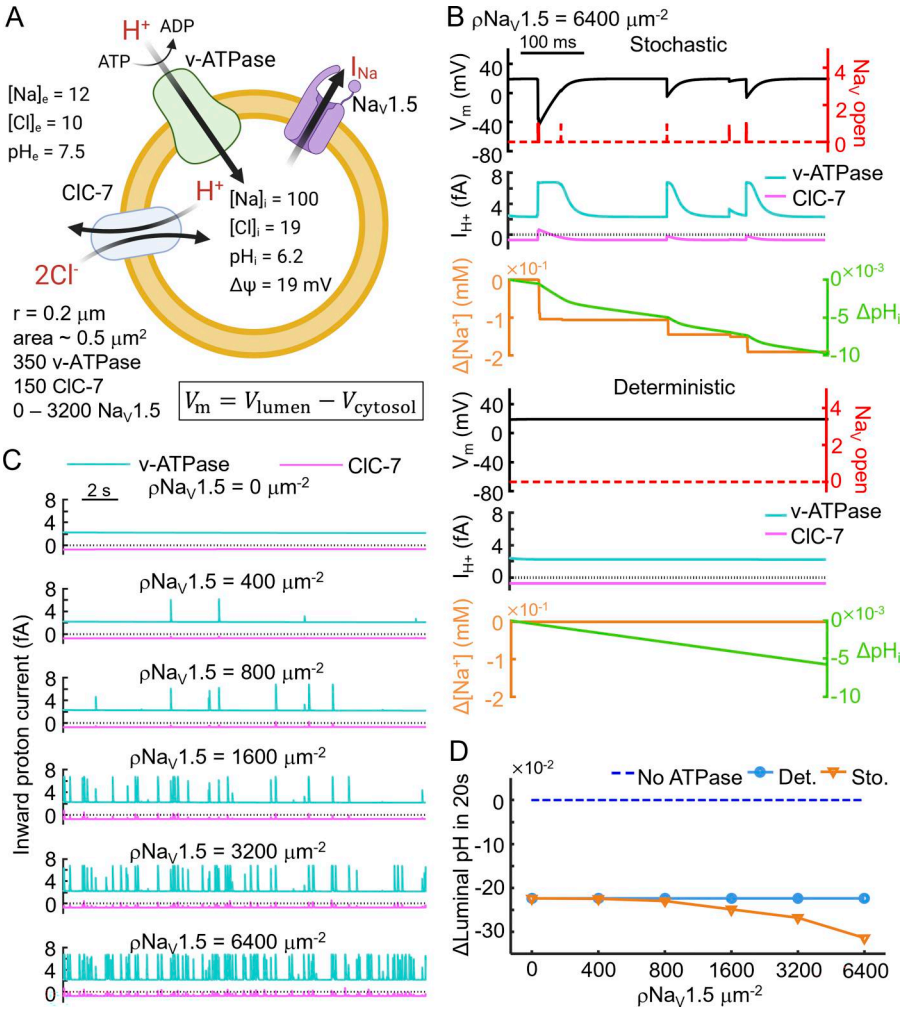

Figure 5. **Stochastic simulations of endosome acidification dynamics. (A)** Model endosome. Concentrations in mM. **(B)** Comparison between the stochastic (top) and deterministic (bottom) dynamics. In the stochastic simulation, spontaneous $Na_V1.5$ fluctuations transiently decreased the membrane voltage and increased the acidification rate. **(C)** The effect of $Na_V1.5$ activity on endosome acidification increased at higher $Na_V1.5$ density. **(D)** Luminal pH in stochastic or deterministic simulations after 20 s, across a range of $Na_V1.5$ channel densities. The initial pH is shown as a dashed line. Created in BioRender. Howell, M. (2025) https://BioRender.com/nm7zk94.

in which N_k is the number of channels in state k and $\alpha_{i\to k}$ is the transition rate from state i to state k ($\alpha_{i\to i} = 0$). Transition rates for all voltage-gated ion channels are provided in Supplemental text, Notes S1 and S2.

The Gillespie method is used for the stochastic simulations (Gillespie, 1977; Chow and White, 1996). In short, we define the sum of all the transition rates across all channels in a system as λ

$$\lambda = \sum_k \left(\sum_i \alpha_{k\to i} N_k \right) \quad \text{M13}$$

Then the probability that no transition occurs in the system after time t follows an exponential distribution

$$P(t) = \lambda \exp[-\lambda t] \quad \text{M14}$$

A random number is drawn from this distribution to determine the time elapsed before the next transition. Then, a uniform random number is drawn to determine which type of transition in which type of channel occurs, with weight $\alpha_{k\to i}\frac{N_k}{\lambda}$ assigned to each type of transition.

Ion concentration update

The deterministic and stochastic Markovian simulations are performed with intravesicular ion concentrations either fixed or continuously updated. The dynamic ion simulations follow the formalism of Hübel and Dahlem (Hübel and Dahlem, 2014; Hübel et al., 2014). The ionic currents are converted to changes in internal and external concentrations, and the reversal potentials of each ionic species are updated accordingly. For all simulations, the external volume is set to 10^5 μm³; large enough that extravesicular ion concentrations are approximately constant. The ionic composition of the applied current is set proportional to the extravesicular cation ratio. For endosome simulations, a buffering capacity of 40 $\frac{mM}{dpH}$ is assumed in updating the intravesicular H^+ concentration, following literature precedent (Grabe and Oster, 2001).

Dynamic choice of simulation step size

To accommodate vesicle sizes and ion channel densities that vary across orders of magnitude, the simulation step size, dt, is chosen dynamically at each step, to satisfy the following criteria: (1) dt <0.001 ms; (2) $dt < 0.2\,\tau_V$, where τ_V is the characteristic membrane charging time; and (3) in a single step, the internal concentration of each ion does not change by >2%.

In driven stochastic simulations, if dt chosen from the exponential distribution exceeds the limits set by (1), (2), or (3), then the transition is rejected, and the system evolves by the time step dictated by (1), (2), or (3).

In simulations of spontaneous activity in single-channel and HH-type vesicles, constraint (1) was relaxed. This minimized the number of timesteps sampled during quiescent periods in vesicles with few channels. Additionally, in simulations of single-channel vesicles without [ion] update, constraint (3) did not apply and (2) was tightened such that $dt < 0.01\,\tau_V$. This enabled accurate calculation of time-averaged V_m.

Vesicle sizes and channel densities

For the HH-type vesicle model, a range of physiologically relevant vesicle sizes and ion channel densities were considered (Fig. 3 B). The vesicle radii were selected to correspond approximately to a synaptic vesicle (r = 0.02 µm) (Murk et al., 2003; Takamori et al., 2006); an endosome (r = 0.05 µm) (Murk et al., 2003); a large endosome or vacuole (r = 0.4 µm) (Ganley et al., 2004); a prokaryotic cell (r = 1 µm); and a eukaryotic cell (r = 10 µm). Ion channel densities were selected as follows: [Na_V K_V] = [80 20] µm^{-2} is the approximate density on the squid giant axon (Chow and White, 1996; Hübel et al., 2014), and [Na_V K_V] = [800, 200] µm^{-2} is the approximate density on a synaptic vesicle if it contains exactly one copy of the K_V. On a synaptic vesicle, the copy numbers of each type of ion channel and transporter are often in the single-digit regime (Daniels et al., 2006; Takamori et al., 2006; Mutch et al., 2011; Farsi et al., 2016; Upmanyu et al., 2022). The ratio of Na_V to K_V was fixed at 4 to 1 across all channel density scales.

For the endosome model, the vesicle radius was 0.2 µm. There are large variations in literature estimates of endosomal v-ATPase density. Patch-clamp measurements on plant vacuoles indicated a density of 700 µm^{-2} (Grabe et al., 2000). Single-molecule photobleaching measurements in HeLa cell lysosomes reported ∼1.5 v-ATPase per lysosome (Maxson et al., 2022). For r = 0.2 µm, this corresponds to a density of ∼3 µm^{-2}. We selected the larger density (700 µm^{-2}) because our model based on this density produced initial acidification rates (∼0.6–0.9 ΔpH/min, Fig 5 D) similar to those recorded in rat liver endosomes (∼0.6–1.1 ΔpH/min) (Van Dyke and Belcher, 1994; Maxson et al., 2022). The density of ClC-7 was adjusted to 300 µm^{-2} to achieve an initial membrane potential of +19 mV (V_{lumen}–$V_{cytosol}$) (Koivusalo et al., 2011; Ishida et al., 2013). The density of $Na_V1.5$ on macrophage late endosomes is not known. We varied this density across a wide range, from 0 to 6,400 µm^{-2}.

Online supplemental material

Supplemental text at the end of the PDF includes a description of the HH-type Na_V, HH-type K_V, and $Na_V1.5$ gating models (Notes S1 and S2). Fig. S1 shows the voltage dependence of steady-state open probability, transition rate constants, and transition time constants for the HH-type Na_V model. Fig. S2 compares the distribution of open-state dwell times from spontaneous gating trajectories of vesicles with a single Na_V to the distribution of open-state lifetimes of vesicles with a single Na_V initialized in the open state. Fig. S3 compares the distribution of closed-state dwell times in r = 0.1 µm and r = 10 µm vesicles with a single Na_V. Tables S1 and S2 list parameters and initial conditions for simulations of HH-type Na_V and K_V ensembles as well as $Na_V1.5$-expressing endosomes.

Results

Scaling electrophysiology to small systems

Single-channel perturbations to membrane voltage

We begin by examining the relationship between membrane voltage and channel dynamics in small systems. Fig. 1 A depicts the scale of several electrically excitable biological systems. For simplicity, we consider a spherical membrane-bound compartment (a "vesicle") containing a single ion channel of type a, with open-state conductance g_a (pS) and reversal potential E_a (mV). Assume the membrane has a specific leak conductance G_0 (pS/µm^2) and a resting potential E_{Leak} (mV). Typically G_0 ∼1 pS/µm^2 for neuronal membranes (Hübel and Dahlem, 2014). What is the effect of the single channel opening on the membrane potential, V_m?

If we approximate all the conductances as Ohmic, then a simple circuit analysis shows that (for static ion concentrations, i.e., fixed ion reversal potentials) the change in steady-state membrane potential upon channel a opening is

$$\Delta V_{ss} = \frac{g_a(E_a - E_0)}{g_a + A\,G_0} \quad [1]$$

where A is the surface area of the vesicle. For example, when $g_a = A\,G_0$, the voltage swing is half its maximum value: $\Delta V_{ss} = (E_a - E_0)/2$. Not surprisingly, the single-channel gating has a substantial effect on the steady-state membrane potential when the unit conductance surpasses the resting leak conductance. Fig. 2 A illustrates this scenario for a canonical HH Na_V.

The leak conductance of a vesicle is proportional to its surface area (assuming a high density of leak channels), while the single-channel conductance is independent of the vesicle surface area. Hence, the crossover between charging regimes (i.e., when $g_a = A\,G_0$) corresponds to a characteristic vesicle radius, r_c. For example, for G_0 = 1 pS/µm^2 and a Na_V (g_a = 14 pS) (Bezanilla, 1987), the crossover radius is r_c = 1.1 µm. For a BK calcium-activated potassium channel (g_a ∼200 pS) (Marty, 1981), r_c = 4 µm, while for a homomeric 5-HT_{3A} receptor (g_a = 1 pS) (Hales et al., 2006), r_c = 280 nm.

Upon opening of a single ion channel (Fig. 2 A), the RC time constant for the voltage to approach its new steady state is

$$\tau_V = \frac{C_M}{g_a + A\,G_0} \quad [2]$$

where $C_M = A\,c_0$ is the membrane capacitance (specific capacitance c_0 ∼10 fF/µm^2), and the denominator is the total membrane conductance. At the crossover radius r_c defined above, $\tau_V = \tau_{mem}/2$, where $\tau_{mem} = c_0/G_0$ is the intrinsic membrane time constant. For example, for G_0 = 1 pS/µm^2, τ_{mem} = 10 ms and when $r = r_c$, τ_V = 5 ms. If the single-channel gating events have duration $\tau_{open} \gg \tau_V$, then ΔV_m approaches ΔV_{ss} during a single gating event (Fig. 2 A, blue trace). If $\tau_{open} \ll \tau_V$, then the amplitude of the voltage fluctuations is suppressed to $\Delta V_m \approx \Delta V_{ss}\tau_{open}/\tau_V$ (Fig. 2 A, yellow trace).

For big vesicles ($r \gg r_c$), single-channel gating changes steady-state voltage by $\Delta V_{ss} \approx \frac{g_a(E_a - E_0)}{A\,G_0}$, with time constant $\tau_V \approx \tau_{mem}$. Since $g_a \ll A\,G_0$ for big vesicles, ΔV_{ss} is a small perturbation to the resting potential (Fig. 2 A, orange trace). This corresponds to the situation previously analyzed in models of

channel stochasticity in neural firing (White et al., 1998; White et al., 2000; Mino et al., 2002; Schmid et al., 2003; Goldwyn and Shea-Brown, 2011).

For small vesicles ($r \ll r_c$), single-channel gating brings the voltage close to the reversal potential of channel a, i.e., $\Delta V_{ss} \approx (E_a - E_0)$. In this case, the time constant is $\tau_V \approx \frac{A\, c_0}{g_a} \ll \tau_{mem}$. For example, upon activation of a single 14 pS channel in a vesicle of r = 0.1 μm, the voltage responds with a time constant $\tau_V \approx 10^{-4}$ s (Fig. 2 A, blue trace). When the channel closes, the voltage relaxes back toward the resting potential with a time constant τ_{mem}.

Thus, for sufficiently small structures, the single-channel influence on the membrane voltage can be substantial, and the membrane voltage equilibrates faster than the characteristic channel gating times (Fig. 2 B). Single ion channels then "see" their own influence on V_m during a stochastic gating event. This self-action changes the statistics of channel fluctuations.

For example, consider a vesicle containing a single Na_V (Na_V model in Fig. S1) and a constitutively open "leak" conductance. Here, we assume internal ion concentrations are fixed (an assumption relaxed later), and we initialize the channel in the open state at $V_m = E_{Leak}$. In a large vesicle, Na_V opening (gating variables m^3: 0 → 1; h: 1) is quickly reversed through deactivation (m^3: 1 → 0). In a small vesicle, Na_V opening depolarizes the vesicle to a voltage which favors the open state. The channel then remains open until open-state inactivation sets in (h: 1 → 0). Closing of the channel leads to an increase in the membrane time-constant from τ_V to τ_{mem}, so the voltage recovery is slower than the voltage upstroke. Fig. 2 C shows how voltage self-action prolongs mean Na_V open-state lifetimes in small vesicles relative to large vesicles, and Fig. S2 shows the underlying distributions of Na_V open times in small and large vesicles.

In a large vesicle, channel closing after an open-state fluctuation typically resets the gating variables to $m^3 = 0$, $h = 1$. The channel is immediately available to open again. Since single-channel gating has minimal effect on V_m (Fig. 2 B, bottom), the channel has a constant probability of opening per unit time. Thus, the closed-state waiting-time distribution is exponentially distributed at short times. Occasionally, open-state fluctuations terminate in an inactivated state ($h = 0$). These rare events lead to a long exponential tail to the waiting time distribution (Fig. 2 D).

In a small vesicle, an open-state fluctuation induces a large depolarization, which continues to act after the channel has inactivated ($h = 0$). The voltage then relaxes back toward E_{Leak} with time constant τ_{mem} (Fig. 2 B, top). The time-dependent voltage interacts with the voltage-dependent gating parameters to produce a complex waiting-time distribution (Fig. 2 D). As a result of the residual depolarization following an open event, the time-average membrane voltage is more depolarized in small vesicles than in large vesicles (Fig. 2 E).

If the resting potential, E_{Leak}, is hyperpolarized relative to E_{Window}, the window current regime is wide enough, and the repolarization is slow enough, then the channel may have a high probability to reopen when the voltage nears E_{Window} (Fig. 2 F, green trace). In trajectories simulated with a Na_V model modified to have a large window current, we observed voltage oscillations between E_{Window} and E_{Na}. Occasionally the voltage repolarized below E_{Window} without the channel opening, leading to a quiescent epoch with voltage close to E_{Leak} (Fig. 2 G, green trace). A spontaneous opening event would then restart the oscillatory dynamics. The membrane voltage thus "chattered" between epochs at E_{Leak} and oscillations between E_{Window} and E_{Na} (Fig. 2, F and G, green trace). This behavior was absent in large vesicles containing the same Na_V model. In a Na_V model modified to have negligible window current (Fig. 2 F, purple trace), the voltage repolarized completely to E_{Leak} (Fig. 2 G, purple trace). Fig. S3 shows the distributions of Na_V closed times for these different scenarios. Through large V_m fluctuations and slow membrane voltage repolarization, small vesicles endow channels with a memory of prior gating events, which can lead to a rich repertoire of vesicle size-dependent dynamics.

Single-channel perturbations to concentration

Stochastic channel gating can also affect the ionic contents of the vesicle. To change the membrane voltage by an amount ΔV requires a flux of charge $\Delta Q = C\Delta V$. The ions carrying this charge flow into an internal volume M. Thus, the change in concentration, $\Delta\Gamma = C\Delta V/(z\,F\,M)$, where z is the valence of the charge carrier and F is the Faraday constant. For a spherical vesicle of radius r, we have $C \propto r^2$ while $M \propto r^3$, so $\Delta\Gamma \propto 1/r$, i.e., for a given voltage swing, changes in internal concentration are bigger for smaller vesicles. Numerically, the change in concentration is $\Delta\Gamma = 3.1 \times 10^{-4}\, \Delta V/z\, r$, where V is measured in mV, r in microns, and Γ in mM. For an r = 0.1 μm vesicle with a voltage swing ΔV = 100 mV, the change in concentration due to charging is ∼0.3 mM/z, likely important only for Ca^{2+}.

This estimate misses an important factor, however. Simultaneous opening of channels with different reversal potentials leads to steady-state ionic flows. Net current can be approximately zero (so $dV/dt \approx 0$), while distinct ionic species maintain equal and opposite flows, e.g., via balanced Na^+ influx and K^+ efflux, leading to substantial changes in concentration.

For example, the increases in lumenal Na^+, $\Delta[Na^+]_i$, caused by single-channel gating events in Fig. 2 A have contributions from both gating charge and steady-state leak current. In these cases, the fractional changes were small: 3% ($r = 0.1\,\mu m$), 0.1% ($r = 1\,\mu m$), and 2×10^{-4}% ($r = 10\,\mu m$) of baseline $[Na^+]_i$. Here, the changes in $[Na^+]_i$ were small because the leak conductance was small and the Na_V open times were short. However, over longer times or when more than one conductance is substantial, the fractional changes in internal concentrations can be large.

In Appendix 1, we analyze this scenario for a persistent Na^+ current combined with a leak conductance. We assume that voltage equilibrates fast compared with $[Na^+]_{in}$. This assumption then leads to a rate of change of $[Na^+]_{in}$ proportional to the difference in reversal potential between Na^+ and the leak

$$\frac{d[Na^+]_{in}}{dt} = \left(\frac{g_{Na} g_{Leak}}{g_{Na} + g_{Leak}}\right) \frac{1}{MzF} \left(E_{Na}(t) - E_{Leak}(t)\right) \qquad [3]$$

where $E_{Na}(t)$ and $E_{Leak}(t)$ are instantaneous values of the Na^+ and leak reversal potentials, respectively. The steady-state $[Na^+]_{in}$ is reached when $E_{Na}(t) = E_{Leak}(t)$. Imposing electroneutrality, i.e., $\frac{d[Na^+]_{in}}{dt} = -\frac{d[X]_{in}}{dt}$, where $[X]_{in}$ is the concentration of the

counterion carried by the leak conductance (e.g., Cl^- or K^+), the steady-state value of $[Na^+]_{in}$ is

$$[Na^+]_{in}(\infty) = [Na^+]_{in}(0) + \frac{[Na^+]_{ext}[X]_{in}(0) - [X]_{ext}[Na^+]_{in}(0)}{[Na^+]_{ext} + [X]_{ext}} \quad [4]$$

where $[X]_{in}(0)$ and $[Na^+]_{in}(0)$ are initial internal concentrations of ions. The external concentrations of ions, $[Na^+]_{ext}$ and $[X]_{ext}$ are assumed to be fixed. From Eq. 3, we derive the characteristic timescale of changes in $[Na^+]_{in}$

$$\tau_{conc} = MzF\frac{(g_{Na} + g_{Leak})}{g_{Na}g_{Leak}}\left(\frac{[Na^+]_{in}(\infty) - [Na^+]_{in}(0)}{E_{Na}(0) - E_{Leak}(0)}\right) \quad [5]$$

where $E_{Na}(0)$ and $E_{Leak}(0)$ are the initial values of the Na^+ and leak reversal potentials, respectively.

Let us consider the case where a single Na_V (g_{Na_V} = 14 pS, E_{Na} = 40 mV) and a single K_V (e.g., a delayed rectifier K^+ channel, g_{K_V} = 20 pS, E_K = −90 mV) are open simultaneously. Then the initial steady-state voltage is −36 mV, the initial steady-state Na^+ current is I_{Na} = −1.1 pA, and the initial steady-state K^+ current is I_K = +1.1 pA. In a 1 µm diameter vesicle, these currents correspond to $\frac{d[Na^+]_{in}}{dt}$ = 21 mM/s. In a 0.1 µm diameter vesicle, $\frac{d[Na^+]_{in}}{dt}$ is 1,000-fold higher, i.e., 21 mM/ms. Thus, a millisecond-duration flicker comprising counter-propagating ionic currents can substantially change the ionic content of a small compartment. Fig. 3 A shows an example of $[Na^+]_{in}$ dynamics resulting from a charging current $\left(I_{Na} = -C_M\frac{dV}{dt}\right)$ and a persistent current $\left(I_{Na} = -C_M\frac{dV}{dt} - I_K\right)$ during Na_V and K_V gating in a small vesicle.

Electrophysiology in HH-type model vesicles

Next, we explore how ion channel stochasticity, self-action on membrane voltage, and ion concentration dynamics interact to influence electrophysiology in small compartments. We modeled small spherical vesicles with variable densities of HH-type Na_V and K_V's (Fig. 3 A, Materials and methods). For biologically plausible vesicle sizes and channel densities, channel numbers vary by ∼7 orders of magnitude (Fig. 3 B). To restore ionic gradients, we added a Na^+/K^+-ATPase with a biophysically realistic Na^+ and K^+ concentration-dependent pumping rate (Barreto and Cressman, 2011; Hübel et al., 2014). We added Na^+, K^+, and Cl^- leak conductances to set a resting potential of −68 mV. The Na^+/K^+-ATPase and the leaks were proportional to the membrane area and deterministic. We simulated voltage and concentration dynamics, comparing deterministic and probabilistic Markov models of Na_V and K_V gating (see Materials and methods). In all simulations, we treated internal ion concentrations as dynamic and external ion concentrations as approximately constant.

Spontaneous activity

We simulated trajectories of spontaneous Na_V and K_V gating. As expected, the deterministic simulations produced no spontaneous activity, since both Na_V and K_V channels remained closed at the resting membrane potential, −68 mV. In stochastic simulations, however, Na_V and K_V channels occasionally fluctuated to the open state. The consequences of these fluctuations depended on vesicle size and channel density.

In small vesicles ($r < 100$ nm), a single Na_V opening could depolarize the vesicle enough to activate other Na_V's, leading to a spike (Fig. 3 C). The spike waveforms were highly variable, due to the strong contributions of discrete channel gating events. During some spikes, the Na_V and K_V currents overlapped, driving rapid ion gradient depletion (Fig. 3 C, inset, right panel). The amount of ion gradient depletion depended on the overlap of the Na_V and K_V open times. Smaller vesicles supported longer Na_V openings due to voltage self-action (Fig 2 C), and higher channel densities created more opportunity for Na_V and K_V overlap. This gradient depletion caused a long-lasting decrease in vesicle excitability, restored eventually by the activity of the Na^+/K^+-ATPase (we assume a constant supply of ATP). This depletion-mediated refractory period is distinct from a typical refractory period associated with ion channel recovery kinetics. Gradient depletion diminished spontaneous spike frequency at high channel densities (Fig 3, F and G, right column).

In larger vesicles (100 nm < r < 1 µm), single-channel events typically induced subthreshold depolarization (Na_V) and hyperpolarization (K_V). As channel density increased, these independent single-channel events began to overlap in time, leading to voltage dynamics that resembled an Ornstein–Uhlenbeck process, i.e., diffusion in a parabolic potential. In other words, stochastic channel events drive voltage fluctuations, while passive membrane leak restores the membrane potential toward its resting value. This scenario has previously been studied analytically (Chow and White, 1996) and numerically (Skaugen and Walløe, 1979). When the biased random walk of voltage approached the Na_V activation potential, it triggered spikes which resembled classical action potentials (Fig 3, D and E). The frequency of these events has been modeled as a Kramers escape process (Chow and White, 1996).

At constant channel density, the spontaneous firing rate showed a non-monotonic dependence on vesicle size (Fig 3 F). For small vesicles, an increase in size led to an increase in the number of channels. Since a single stochastic channel gating event was sufficient to trigger a spike, more channels led to a higher spontaneous spike rate. For large vesicles, the influence of single-channel gating events on membrane voltage decreased, so spontaneous spikes became less frequent. This non-monotonic trend is similar to results of numerical simulations by Skaugen and Walløe (Skaugen and Walløe, 1979). The largest vesicles (r > 1 µm) were quiescent at all but the highest channel densities.

Evoked activity

We next simulated voltage trajectories in response to constant current injection. To mimic the effect of an electrogenic pump (optogenetic or chemically driven), we made the current proportional to membrane area ($I \approx 2.4 \times 10^3$ fA/µm^2). We generated voltage trajectories using both stochastic and deterministic (i.e., HH-like) simulations of channel gating with dynamic internal ion concentrations.

When the number of channels was small, discrete gating events led to substantial deviations between the deterministic and stochastic simulations. Stochastic gating events could lead to spontaneous recovery from depolarization block (Fig. 4 A), and

converted regular spike trains into irregular trains (Fig. 4 B). As channel number increased, stochastic trajectories came to resemble deterministic trajectories of the same vesicle (Fig. 4 C). We quantified the similarity between voltage traces for deterministic vs. stochastic simulations via rmsd between the autocorrelation functions of the two voltage trajectories (see Materials and methods). Fig. 4 D shows the similarity between deterministic and stochastic simulations as a function of vesicle size and channel density.

We quantified the extent of internal ion concentration changes in the stochastic simulations. The ion gradients were more prone to depletion when the vesicle was smaller and the channel density was higher, as in the simulations in the absence of current injection (Figs 3 G and 4 E).

$Na_V1.5$ channels and endosome acidification

Finally, we modeled the effects of small-scale electrophysiology on macrophage endosome acidification. This acidification is essential for the killing of pathogens engulfed by phagocytosis. Macrophage endosomes express $Na_V1.5$, with C-terminus outside the lumen (inverted relative to $Na_V1.5$ on the cell membrane). The channel density in endosomes is not known (Carrithers et al., 2007), so we simulated vesicles with $Na_V1.5$ densities (ρ_{Na_V}) between 0 and 6,400 μm^{-2}. We assumed radius r = 0.2 μm (Ganley et al., 2004) (Fig. 5 A), initial membrane potential +19 mV (inside relative to outside), initial pH 6.2, and initial internal Na^+ concentration 100 mM (Koivusalo et al., 2011; Scott and Gruenberg, 2011). A v-ATPase imports H^+, acidifying the endosome during maturation (Grabe et al., 2000; Ishida et al., 2013), and ClC-7 contributes a small outward H^+ current (Ishida et al., 2013). The electrophysiological parameters and initial conditions are in Table S2. The $Na_V1.5$ model is described in Supplemental text, Note S2. The endosomal $Na_V1.5$ model accounts for isoform-specific features, including greater steady-state inactivation at moderate to high voltages compared with the canonical HH Na_V model.

In deterministic simulations of endosomes with $\rho_{Na_V} = 6,400\,\mu m^{-2}$, the mean number of open $Na_V1.5$ channels was always < 1. We rounded the Na_V conductance to the nearest integer (in units of the open-state conductance), which rounded to zero. Hence, the Na_V's did not contribute to the deterministic simulations (Fig. 5 B).

In stochastic simulations at $\rho_{Na_V} = 6,400\,\mu m^{-2}$, the $Na_V1.5$ channels were mostly in the inactive state due to the "felt" voltage of −19 mV (outside relative to inside). Occasionally, a single $Na_V1.5$ channel fluctuated to the open state. In the r = 0.2 μm vesicle, this induced a decrease in membrane voltage (inside relative to outside) of ∼21 ± 16 mV (mean ± SD) since $[Na^+]$ was higher inside the endosome than in the cytoplasm. The voltage dips recovered with a time constant of ∼16 ± 2.4 ms (mean ± SD). The voltage decrease enhanced v-ATPase activity and suppressed the outward H^+ current due to ClC-7 activity, speeding up acidification (Fig. 5 B). The effect of $Na_V1.5$ activity on the acidification dynamics became more pronounced as $Na_V1.5$ channel density increased, since the fraction of time when there was one $Na_V1.5$ channel open was proportional to the number of $Na_V1.5$ channels present (Fig. 5 C).

Fig. 5 D shows endosomal pH change as a function of the density of $Na_V1.5$ channels. In the deterministic simulations, the acidification rate was unaffected by the presence of $Na_V1.5$, since the average number of open channels was approximately zero. In the stochastic simulations, however, the acidification rate increased as $Na_V1.5$ channel density increased, due to the Na_V-induced membrane potential fluctuations. Thus, stochastic channel fluctuations are likely relevant to this important physiological process.

Discussion

This work identifies a qualitative regime change in electrophysiology as membrane-enclosed compartments shrink to submicron dimensions. In this regime, (1) single-channel openings can drive large, rapid excursions in membrane potential, (2) the resulting voltage changes feed back onto channel kinetics during the same opening event, and (3) ionic currents—especially counter-propagating currents through different channel types—can measurably reshape intralumenal ion concentrations during single gating events. By combining Markov-state channel gating with self-consistent voltage dynamics and ion-concentration updates, we provide a unified framework that connects classical conductance-based descriptions to the single-molecule limit.

A central implication of our work is that small compartments need not behave like miniature versions of excitable cells. In the classical setting (large membrane area and many channels), channel noise is well captured as an approximately Gaussian perturbation around a mean conductance, enabling diffusion/Langevin and Kramers-type descriptions of rare excursions and spontaneous spikes (Skaugen and Walløe, 1979; Chow and White, 1996; White et al., 1998; White et al., 2000; Mino et al., 2002; Schmid et al., 2003; Faisal et al., 2005; Goldwyn and Shea-Brown, 2011; Schmandt and Galán, 2012). In contrast, when channel copy numbers are in the single-digit to tens, and leak conductance and capacitance are correspondingly small, voltage trajectories are inherently jump-like: individual gating events can move V_m a substantial fraction of the way toward a reversal potential, and the ensuing self-action can prolong or curtail dwell times depending on the voltage-dependence of the transition rates. Though the joint dynamics of channel-state and membrane voltage remain Markovian (i.e., memoryless), the slow voltage variable gives the channel dynamics an apparent memory, i.e., gating probabilities depend on the specific trajectory of past stochastic gating events. These memory effects can generate dynamics—such as intermittency or "chattering" in channels with appreciable window currents—that have no direct analog in larger systems.

A second implication concerns ionic homeostasis. In large cells, voltage dynamics are often computed with fixed reversal potentials (except for Ca^{2+}), and concentration dynamics enter only as slow modulators (DiFrancesco and Noble, 1997; Hübel and Dahlem, 2014). In small volumes, this separation can break down. Our simulations highlight a particularly important case: coincident opening of conductances with different reversal potentials can drive large counter-propagating ionic fluxes

while producing little net capacitive current. This flux can rapidly dissipate Na^+/K^+ gradients, producing a depletion-mediated refractory period that is mechanistically distinct from classic refractoriness set by channel inactivation and recovery.

This predicted mechanism suggests a plausible interpretation for recent organelle measurements. For example, in endosomes, heterogeneity in lumenal Na^+ and maturation-dependent shifts in lumenal Na^+ together suggest that intralumenal Na^+ may be a more dynamic quantity than in large cells (Zou et al., 2024). Similarly, K^+ channel activity in trafficking organelles measurably changes lumenal K^+, also suggesting a dynamic role for lumenal K^+ (Anees et al., 2024). Our results motivate the hypothesis that some of the observed heterogeneity could arise from rare overlaps of channel openings that transiently reshape ionic gradients. Simultaneous imaging of organellar ion content (Saha et al., 2015; Anees et al., 2024; Zou et al., 2024) and membrane voltage (e.g., via fluorescence lifetime imaging of a voltage-sensitive dye), together with channel pharmacology, would be a promising approach toward characterizing the interplay of channel gating, ionic concentrations, and voltage. Experiments in synthetic vesicles of known composition could test the biophysical ideas without the uncertainty in channel content that arises in native vesicles.

Although not explicitly considered here, discrete fluctuations in free lumenal ions create an additional source of stochastic noise in ion homeostasis. Such considerations become important for species which are highly buffered, e.g., cytosolic $[H^+]$ ~60 nM and cytosolic $[Ca^{2+}]$ ~100 nM, and in the smallest compartments, such as a synaptic vesicle (r = 0.02 μm), where the difference of a single ion corresponds to a ~50 μM difference in lumenal concentration. The degree to which such fluctuations impact compartment ionic set-points depends heavily on local buffer parameters (Singh et al., 2019).

Our endosome simulations provide a complementary example of how discrete gating can matter even when the mean open probability is extremely small. For $Na_V1.5$ in macrophage late endosomes (Carrithers et al., 2007), the deterministic (mean-field) description can effectively "round away" the channel contribution when the expected number of open channels is $\ll 1$. The stochastic model, however, predicts that rare single-channel openings can generate transient voltage excursions that systematically bias electrogenic transport (v-ATPase, ClC-7), accelerating acidification. This points to a broader principle: in nanoscale compartments, physiological impact may be controlled by event statistics (amplitude, dwell-time distributions, and coincidence rates) rather than by ensemble- or time-averaged conductances.

These considerations suggest several experimentally testable predictions and design principles for organelle and microbial electrophysiology. First, voltage and ion measurements at single-organelle resolution (Saminathan et al., 2021; Anees et al., 2024; Zou et al., 2024) should exhibit non-Gaussian signatures—e.g., heavy-tailed distributions of voltage deflections and state-dependent dwell times—that become more distinct as compartments become smaller or channel copy number decreases. Second, simultaneous measurements of V_m and lumenal counterions (e.g., $[Na^+]$ or pH in endosomes) should reveal transient covariance consistent with counter-propagating flux episodes: large voltage events with disproportionately large concentration changes when multiple channel types overlap. Third, perturbations that change organelle size, channel abundance, or kinetics (e.g., channel blockers or mutants that modify window current) should shift systems between qualitatively distinct dynamical regimes in predictable ways, offering a path to infer otherwise inaccessible parameters such as channel copy number per organelle.

Several extensions could broaden the model's applicability. Many small compartments are not closed: dendritic spines, nodes of Ranvier, and subcellular invaginations exchange ions with a larger reservoir through narrow necks or diffusion-limited pathways (Salzer, 1997; Sabatini and Svoboda, 2000; Harnett et al., 2012). Incorporating diffusive coupling to the cytosol or extracellular space would allow the same framework to address when local ionic depletion is buffered by exchange versus when it becomes functionally consequential. Similarly, allowing external concentrations to vary—important in crowded extracellular spaces where external volume fractions are small—would connect to activity-driven extracellular K^+ accumulation and spreading depolarization phenomena (Somjen, 2001; Dreier, 2011). Finally, while we treated pumps and transporters deterministically, growing evidence indicates that ultraslow mode switching and static disorder can be intrinsic to transport proteins (Ciftci et al., 2020; Kosmidis et al., 2022; Møller et al., 2026, *Preprint*). A fully stochastic treatment of pumps and exchangers, coupled to voltage and concentration dynamics, may be essential for quantitatively predicting organelle-to-organelle heterogeneity and intermittency.

More broadly, this work emphasizes that "channel noise" in small compartments can be a primary driver of state transitions and homeostatic set points. As optical electrophysiology and organelle-resolved ion sensing mature (Modi et al., 2009; Saha et al., 2015; Narayanaswamy et al., 2019; Saminathan et al., 2021; Anees et al., 2024; Zou et al., 2024), theories that retain discreteness—single-molecule gating, finite copy numbers, and concentration-driven feedback—will be increasingly necessary for interpretation and for mechanistic inference from data.

Appendix: Effect of single-channel gating on ion concentrations

For concreteness we consider a persistent Na^+ current, though the discussion applies to any persistent current. The membrane voltage, V_m, evolves according to:

$$\frac{dV_m}{dt} = -\frac{1}{C_M}\left(i_{Na}(t) + i_{Leak}(t)\right) \quad \text{A1}$$

where $i_{Na}(t)$ is the inward Na^+ current, $i_{Leak}(t)$ is the outward leak current, and C_M is the membrane capacitance. The rate of change of concentration of Na^+ inside the vesicle is

$$\frac{d[Na^+]_{in}}{dt} = -\frac{i_{Na}(t)}{M\,z\,F} \quad \text{A2}$$

where, M is the vesicle volume, z is the valence (1 for Na^+) and F is the Faraday constant. The Na^+ current is

$$i_{Na}(t) = g_{Na}(V_m(t) - E_{Na}(t)) \quad \text{A3}$$

For clarity, we make the time-dependencies explicit and define g_x as the channel's open-state conductance and $E_x(t)$ as the channel's reversal potential; x = Na^+ or leak ion. We assume that the voltage is in a local equilibrium (i.e., voltage changes are fast compared to the concentrations). Solving Eq. A1 for the steady-state voltage, $V_{ss}(t)$:

$$V_{ss}(t) = \frac{g_{Na}E_{Na}(t) + g_{Leak}E_{Leak}(t)}{g_{Na} + g_{Leak}} \quad \text{A4}$$

Setting $V_m(t) = V_{ss}(t)$ in Eq. A3 and combining Eqs. A2 and A3 gives

$$\frac{d[Na^+]_{in}}{dt} = \left(\frac{g_{Na}g_{Leak}}{g_{Na} + g_{Leak}}\right)\frac{1}{MzF}(E_{Na}(t) - E_{Leak}(t)) \quad \text{A5}$$

Finally, the Na^+ reversal potential changes with time as the internal concentration changes

$$E_{Na} = \frac{RT}{zF}\ln\frac{[Na^+]_{out}}{[Na^+]_{in}(t)} \quad \text{A6}$$

Combining Eqs. A5 and A6 gives an expression for the dynamics of $[Na^+]_{in}$:

$$\frac{d[Na^+]_{in}}{dt} = \left(\frac{g_{Na}g_{Leak}}{g_{Na} + g_{Leak}}\right)\frac{1}{MzF}\left(\frac{RT}{zF}\ln\frac{[Na^+]_{out}}{[Na^+]_{in}(t)} - E_{Leak}(t)\right) \quad \text{A7}$$

In the case where $g_{Leak} \propto r^2$ and $M \propto r^3$ (i.e., a constant leak conductance per unit membrane area in a spherical vesicle), then $\frac{d[Na^+]_{in}}{dt} \propto -\frac{1}{r}$ for small vesicles ($g_{Na} \gg A\,G_0$) and $\frac{d[Na^+]_{in}}{dt} \propto -\frac{1}{r^3}$ for large vesicles ($g^0_{Na} \ll A\,G_0$).

Eq. A7 is nonlinear in $[Na^+]_{in}$ and does not have a closed-form analytical solution. Numerical integration yields the time-dependent trajectory of $[Na^+]_{in}$. An approximate timescale can be estimated by extrapolating the initial rate of change to the entire transition from $[Na^+]_{in}(0)$ to $[Na^+]_{in}(\infty)$, i.e.,

$$\tau_{conc} \approx ([Na^+]_{in}(\infty) - [Na^+]_{in}(0))\Big/\left.\frac{d[Na^+]_{in}}{dt}\right|_{t=0} \quad \text{A8}$$

where

$$\left.\frac{d[Na^+]_{in}}{dt}\right|_{t=0} = \left(\frac{g_{Na}g_{Leak}}{g_{Na} + g_{Leak}}\right)\frac{1}{MzF}(E_{Na}(0) - E_{Leak}(0)) \quad \text{A9}$$

Combining Eqs. A8 and A9 yields Eq. 5 in the main text.

Data availability

Annotated MATLAB code for stochastic simulations of single-channel vesicles, HH-model vesicles, and macrophage endosomes is provided in a publicly accessible GitHub repository: https://github.com/adamcohenlab/howell2025small-scale-ephys. Simulated data and analysis codes are available upon request.

Acknowledgments

Joseph A. Mindell served as editor.

We thank Prof. Michael Grabe of University of California, San Francisco for providing us with the MATLAB code for the vesicle-type H + ATPase model. Components of Figs. 1, 2, 3, 5, and Note S2 were created in BioRender. Howell, M. (2025) https://BioRender.com/nm7zk94.

This work was supported by a National Science Foundation (NSF) Graduate Research Fellowship DGE-2140743 (M.R. Howell) and NSF Quantum Sensing for Biophysics (QuBBe) and Bioengineering Quantum Leap Challenge Institute (QLCI) grant OMA-2121044.

Author contributions: Madeleine R. Howell: conceptualization, formal analysis, investigation, methodology, software, visualization, and writing—original draft, review, and editing. Rosalind J. Xu: conceptualization, data curation, formal analysis, investigation, methodology, software, validation, visualization, and writing—original draft, review, and editing. Adam E. Cohen: conceptualization, formal analysis, funding acquisition, project administration, resources, supervision, visualization, and writing—original draft, review, and editing.

Disclosures: A.E. Cohen reported personal fees from Luminos LLC, Quiver Biosciences, Exin Therapeutics, and Morphoceuticals outside the submitted work. No other disclosures were reported.

Submitted: 24 March 2026
Revised: 10 June 2026
Accepted: 18 June 2026

References

Abdelfattah, A.S., J. Zheng, A. Singh, Y.-C. Huang, D. Reep, G. Tsegaye, A. Tsang, B.J. Arthur, M. Rehorova, C.V.L. Olson, et al. 2023. Sensitivity optimization of a rhodopsin-based fluorescent voltage indicator. *Neuron*. 111:1547–1563.e9. https://doi.org/10.1016/j.neuron.2023.03.009

Adam, Y., J.J. Kim, S. Lou, Y. Zhao, M.E. Xie, D. Brinks, H. Wu, M.A. Mostajo-Radji, S. Kheifets, V. Parot, et al. 2019. Voltage imaging and optogenetics reveal behaviour-dependent changes in hippocampal dynamics. *Nature*. 569:413–417. https://doi.org/10.1038/s41586-019-1166-7

Akole, A., and J.M. Warner. 2019. Model of influenza virus acidification. *PLoS One*. 14:e0214448. https://doi.org/10.1371/journal.pone.0214448

Anees, P., A. Saminathan, E.R. Rozmus, A. Di, A.B. Malik, B.P. Delisle, and Y. Krishnan. 2024. Detecting organelle-specific activity of potassium channels with a DNA nanodevice. *Nat. Biotechnol.* 42:1065–1074. https://doi.org/10.1038/s41587-023-01928-z

Antic, S.D., P. Yan, C.D. Acker, O.T. Spagnola, Z.Y. Erol, O. Baser, and L.M. Loew. 2025. ElectroFluor voltage-sensitive dyes: Comprehensive analysis of wavelength-dependent sensitivity and cross-channel bleed-through. *J. Biophotonics*. 18:e70008. https://doi.org/10.1002/jbio.70008

Armbruster, M., S. Naskar, J.P. Garcia, M. Sommer, E. Kim, Y. Adam, P.G. Haydon, E.S. Boyden, A.E. Cohen, and C.G. Dulla. 2022. Neuronal activity drives pathway-specific depolarization of peripheral astrocyte processes. *Nat. Neurosci.* 25:607–616. https://doi.org/10.1038/s41593-022-01049-x

Balbi, P., P. Massobrio, and J.H. Kotaleski. 2017. A single Markov-type kinetic model accounting for the macroscopic currents of all human voltage-gated sodium channel isoforms. *PLoS Comput. Biol.* 13:e1005737. https://doi.org/10.1371/journal.pcbi.1005737

Barreto, E., and J.R. Cressman. 2011. Ion concentration dynamics as a mechanism for neuronal bursting. *J. Biol. Phys.* 37:361–373. https://doi.org/10.1007/s10867-010-9212-6

Benarroch, J.M., and M. Asally. 2020. The microbiologist's guide to membrane potential dynamics. *Trends Microbiol.* 28:304–314. https://doi.org/10.1016/j.tim.2019.12.008

Berrier, C., M. Besnard, B. Ajouz, A. Coulombe, and A. Ghazi. 1996. Multiple mechanosensitive ion channels from *Escherichia coli*, activated at different thresholds of applied pressure. *J. Membr. Biol.* 151:175–187. https://doi.org/10.1007/s002329900068

Bertl, A., E. Blumwald, R. Coronado, R. Eisenberg, G. Findlay, D. Gradmann, B. Hille, K. Köhler, H.A. Kolb, and E. MacRobbie. 1992. Electrical measurements on endomembranes. *Science*. 258:873–874. https://doi.org/10.1126/science.1439795

Beyder, A., J.L. Rae, C. Bernard, P.R. Strege, F. Sachs, and G. Farrugia. 2010. Mechanosensitivity of Nav1.5, a voltage-sensitive sodium channel. *J. Physiol.* 588:4969–4985. https://doi.org/10.1113/jphysiol.2010.199034

Bezanilla, F. 1987. Single sodium channels from the squid giant axon. *Biophysical J.* 52:1087–1090. https://doi.org/10.1016/S0006-3495(87)83304-0

Cannon, R.C., C. O'Donnell, and M.F. Nolan. 2010. Stochastic ion channel gating in dendritic neurons: Morphology dependence and probabilistic synaptic activation of dendritic spikes. *PLoS Comput. Biol.* 6:e1000886. https://doi.org/10.1371/journal.pcbi.1000886

Carrithers, M.D., S. Dib-Hajj, L.M. Carrithers, G. Tokmoulina, M. Pypaert, E.A. Jonas, and S.G. Waxman. 2007. Expression of the voltage-gated sodium channel NaV1.5 in the macrophage late endosome regulates endosomal Acidification. *J. Immunol.* 178:7822–7832. https://doi.org/10.4049/jimmunol.178.12.7822

Chay, T.R., and J. Keizer. 1983. Minimal model for membrane oscillations in the pancreatic beta-cell. *Biophys. J.* 42:181–189. https://doi.org/10.1016/S0006-3495(83)84384-7

Chow, C.C., and J.A. White. 1996. Spontaneous action potentials due to channel fluctuations. *Biophys. J.* 71:3013–3021. https://doi.org/10.1016/S0006-3495(96)79494-8

Ciftci, D., G.H.M. Huysmans, X. Wang, C. He, D. Terry, Z. Zhou, G. Fitzgerald, S.C. Blanchard, and O. Boudker. 2020. Single-molecule transport kinetics of a glutamate transporter homolog shows static disorder. *Sci. Adv.* 6:eaaz1949. https://doi.org/10.1126/sciadv.aaz1949

Cohen, A.E., and V. Venkatachalam. 2014. Bringing bioelectricity to light. *Annu. Rev. Biophys.* 43:11.1–11.22. https://doi.org/10.1146/annurev-biophys-051013-022717

Cornejo, V.H., N. Ofer, and R. Yuste. 2021. Voltage compartmentalization in dendritic spines in vivo. *Science*. 375:82–86. https://doi.org/10.1126/science.abg0501

Crowley, L.C., M.E. Christensen, and N.J. Waterhouse. 2016. Measuring mitochondrial transmembrane potential by TMRE staining. *Cold Spring Harb. Protoc.* 2016. https://doi.org/10.1101/pdb.prot087361

Daniels, R.W., C.A. Collins, K. Chen, M.V. Gelfand, D.E. Featherstone, and A. DiAntonio. 2006. A single vesicular glutamate transporter is sufficient to fill a synaptic vesicle. *Neuron*. 49:11–16. https://doi.org/10.1016/j.neuron.2005.11.032

Destexhe, A., and J.R. Huguenard. 2009. Modeling voltage-dependent channels. *In* Computational Modeling Methods for Neuroscientists. E. De Schutter, editor. The MIT Press, Cambridge, MA. 107–138. https://doi.org/10.7551/mitpress/9780262013277.003.0006

DiFrancesco, D., and D. Noble. 1997. A model of cardiac electrical activity incorporating ionic pumps and concentration changes. *Philos. Trans. R. Soc. Lond. B, Biol. Sci.* 307:353–398. https://doi.org/10.1098/rstb.1985.0001

Dreier, J.P. 2011. The role of spreading depression, spreading depolarization and spreading ischemia in neurological disease. *Nat. Med.* 17:439–447. https://doi.org/10.1038/nm.2333

Faisal, A.A., J.A. White, and S.B. Laughlin. 2005. Ion-Channel noise places limits on the miniaturization of the brain's wiring. *Curr. Biol.* 15:1143–1149. https://doi.org/10.1016/j.cub.2005.05.056

Farsi, Z., J. Preobraschenski, G. van den Bogaart, D. Riedel, R. Jahn, and A. Woehler. 2016. Single-vesicle imaging reveals different transport mechanisms between glutamatergic and GABAergic vesicles. *Science*. 351:981–984. https://doi.org/10.1126/science.aad8142

Finazzi, G., D. Petroutsos, M. Tomizioli, S. Flori, E. Sautron, V. Villanova, N. Rolland, and D. Seigneurin-Berny. 2015. Ions channels/transporters and chloroplast regulation. *Cell Calcium*. 58:86–97. https://doi.org/10.1016/j.ceca.2014.10.002

Ganley, I.G., K. Carroll, L. Bittova, and S. Pfeffer. 2004. Rab9 GTPase regulates late endosome size and requires effector interaction for its stability. *Mol. Biol. Cell*. 15:5420–5430. https://doi.org/10.1091/mbc.E04-08-0747

Gillespie, D.T. 1977. Exact stochastic simulation of coupled chemical reactions. *J. Phys. Chem.* 81:2340–2361. https://doi.org/10.1021/j100540a008

Goldwyn, J.H., and E. Shea-Brown. 2011. The what and where of adding channel noise to the hodgkin-huxley equations. *PLoS Comput. Biol.* 7:e1002247. https://doi.org/10.1371/journal.pcbi.1002247

Grabe, M., and G. Oster. 2001. Regulation of organelle acidity. *J. Gen. Physiol.* 117:329–344. https://doi.org/10.1085/jgp.117.4.329

Grabe, M., H. Wang, and G. Oster. 2000. The mechanochemistry of V-ATPase proton pumps. *Biophys. J.* 78:2798–2813. https://doi.org/10.1016/S0006-3495(00)76823-8

Hales, T.G., J.I. Dunlop, T.Z. Deeb, J.E. Carland, S.P. Kelley, J.J. Lambert, and J.A. Peters. 2006. Common determinants of single channel conductance within the large cytoplasmic loop of 5-hydroxytryptamine type 3 and alpha4beta2 nicotinic acetylcholine receptors. *J. Biol. Chem.* 281:8062–8071. https://doi.org/10.1074/jbc.M513222200

Hao, Y.A., S. Lee, R.H. Roth, S. Natale, L. Gomez, J. Taxidis, P.S. O'Neill, V. Villette, J. Bradley, Z. Wang, et al. 2024. A fast and responsive voltage indicator with enhanced sensitivity for unitary synaptic events. *Neuron*. 112:3680–3696.e8. https://doi.org/10.1016/j.neuron.2024.08.019

Harnett, M.T., J.K. Makara, N. Spruston, W.L. Kath, and J.C. Magee. 2012. Synaptic amplification by dendritic spines enhances input cooperativity. *Nature*. 491:599–602. https://doi.org/10.1038/nature11554

Hodgkin, A.L., and Huxley, A.F. 1952. A quantitative description of membrane current and its application to conduction and excitation in nerve. *J. Physiol.* 117:500–544. https://doi.org/10.1113/jphysiol.1952.sp004764

Hübel, N., and M.A. Dahlem. 2014. Dynamics from seconds to hours in hodgkin-huxley model with time-dependent ion concentrations and buffer reservoirs. *PLoS Comput. Biol.* 10:e1003941. https://doi.org/10.1371/journal.pcbi.1003941

Hübel, N., E. Schöll, and M.A. Dahlem. 2014. Bistable dynamics underlying excitability of ion homeostasis in neuron models. *PLoS Comput. Biol.* 10:e1003551. https://doi.org/10.1371/journal.pcbi.1003551

Ichas, F., L.S. Jouaville, and J.P. Mazat. 1997. Mitochondria are excitable organelles capable of generating and conveying electrical and calcium signals. *Cell*. 89:1145–1154. https://doi.org/10.1016/s0092-8674(00)80301-3

Ishida, Y., S. Nayak, J.A. Mindell, and M. Grabe. 2013. A model of lysosomal pH regulation. *J. Gen. Physiol.* 141:705–720. https://doi.org/10.1085/jgp.201210930

Johansson, S., and P. Arhem. 1994. Single-channel currents trigger action potentials in small cultured hippocampal neurons. *Proc. Natl. Acad. Sci. USA*. 91:1761–1765. https://doi.org/10.1073/pnas.91.5.1761

Kannan, M., G. Vasan, S. Haziza, C. Huang, R. Chrapkiewicz, J. Luo, J.A. Cardin, M.J. Schnitzer, and V.A. Pieribone. 2022. Dual-polarity voltage imaging of the concurrent dynamics of multiple neuron types. *Science*. 378:eabm8797. https://doi.org/10.1126/science.abm8797

Koivusalo, M., B.E. Steinberg, D. Mason, and S. Grinstein. 2011. In situ measurement of the electrical potential across the lysosomal membrane using FRET. *Traffic*. 12:972–982. https://doi.org/10.1111/j.1600-0854.2011.01215.x

Kosmidis, E., C.G. Shuttle, J. Preobraschenski, M. Ganzella, P.J. Johnson, S. Veshaguri, J. Holmkvist, M.P. Møller, O. Marantos, F. Marcoline, et al. 2022. Regulation of the mammalian-brain V-ATPase through ultraslow mode-switching. *Nature*. 611:827–834. https://doi.org/10.1038/s41586-022-05472-9

Kowaltowski, A.J., and F. Abdulkader. 2024. How and when to measure mitochondrial inner membrane potentials. *Biophys. J.* 123:4150–4157. https://doi.org/10.1016/j.bpj.2024.03.011

Kralj, J.M., D.R. Hochbaum, A.D. Douglass, and A.E. Cohen. 2011. Electrical spiking *in Escherichia coli* probed with a fluorescent voltage-indicating protein. *Science*. 333:345–348. https://doi.org/10.1126/science.120476310/b5czk8

Krishnan, G.P., and M. Bazhenov. 2011. Ionic dynamics mediate spontaneous termination of seizures and postictal depression state. *J. Neurosci.* 31:8870–8882. https://doi.org/10.1523/JNEUROSCI.6200-10.2011

Llano, I., C.K. Webb, and F. Bezanilla. 1988. Potassium conductance of the squid giant axon. Single-channel studies. *J. Gen. Physiol.* 92:179–196. https://doi.org/10.1085/jgp.92.2.179

Lu, X., Y. Wang, Z. Liu, Y. Gou, D. Jaeger, and F. St-Pierre. 2023. Widefield imaging of rapid pan-cortical voltage dynamics with an indicator evolved for one-photon microscopy. *Nat. Commun.* 14:6423. https://doi.org/10.1038/s41467-023-41975-3

Martinac, B., M. Buechner, A.H. Delcour, J. Adler, and C. Kung. 1987. Pressure-sensitive ion channel in *Escherichia coli*. *Proc. Natl. Acad. Sci. USA*. 84:2297–2301. https://doi.org/10.1073/pnas.84.8.2297

Martinac, B., Y. Saimi, and C. Kung. 2008. Ion channels in microbes. *Physiol. Rev.* 88:1449–1490. https://doi.org/10.1152/physrev.00005.2008

Marty, A. 1981. Ca-dependent K channels with large unitary conductance in chromaffin cell membranes. *Nature*. 291:497–500. https://doi.org/10.1038/291497a0

Maxson, M.E., Y.M. Abbas, J.Z. Wu, J.D. Plumb, S. Grinstein, and J.L. Rubinstein. 2022. Detection and quantification of the vacuolar H+ATPase using the Legionella effector protein SidK. *J. Cell Biol.* 221:e202107174. https://doi.org/10.1083/jcb.202107174

McKinney, L.C., and A. Moran. 1995. Regulation of intracellular pH in J774 murine macrophage cells: H+ extrusion processes. *Am. J. Physiol.* 268:C210–C217. https://doi.org/10.1152/ajpcell.1995.268.1.C210

McVeigh, B.M., J.J. De Jesús-Pérez, D.H. Siepe, P. Gogoi, S.K. Mageswaran, M. Kalocsay, E.M. Mihelc, and V.Y. Moiseenkova-Bell. 2025. Visualization of lysosomal membrane proteins by cryo electron tomography. *Nat. Commun.* 16:9234. https://doi.org/10.1038/s41467-025-64314-0

Miller, E.W., J.Y. Lin, E.P. Frady, P.A. Steinbach, W.B. Kristan Jr, and R.Y. Tsien. 2012. Optically monitoring voltage in neurons by photo-induced electron transfer through molecular wires. *Proc. Natl. Acad. Sci. USA*. 109:2114–2119. https://doi.org/10.1073/pnas.1120694109

Mino, H., J.T. Rubinstein, and J.A. White. 2002. Comparison of algorithms for the simulation of action potentials with stochastic sodium channels. *Ann. Biomed. Eng.* 30:578–587. https://doi.org/10.1114/1.1475343

Modi, S., S. M G, D. Goswami, G.D. Gupta, S. Mayor, and Y. Krishnan. 2009. A DNA nanomachine that maps spatial and temporal pH changes inside living cells. *Nat. Nanotechnology*. 4:325–330. https://doi.org/10.1038/nnano.2009.83

Møller, M.P., Cvjetkovic, A., Kosmidis, E., Narducci, A., Isselstein, M., Shuttle, C.G., Justesen, B., Jørgensen, I.L., Basse-Hansen, S., Dyla, M., et al, 2026. Long-term single-molecule Ca2+ flux recordings reveal mode-switching regulation of Ca2+-ATPases. *bioRxiv*. https://doi.org/10.64898/2026.01.28.701947 (Preprint posted January 31, 2026).

Murk, J.L.A. N., B.M. Humbel, U. Ziese, J.M. Griffith, G. Posthuma, J.W. Slot, A.J. Koster, A.J. Verkleij, H.J. Geuze, and M.J. Kleijmeer. 2003. Endosomal compartmentalization in three dimensions: Implications for membrane fusion. *Proc. Natl. Acad. Sci. USA*. 100:13332–13337. https://doi.org/10.1073/pnas.2232379100

Mutch, S.A., P. Kensel-Hammes, J.C. Gadd, B.S. Fujimoto, R.W. Allen, P.G. Schiro, R.M. Lorenz, C.L. Kuyper, J.S. Kuo, S.M. Bajjalieh, and D.T. Chiu. 2011. Protein quantification at the single vesicle level reveals that a subset of synaptic vesicle proteins are trafficked with high precision. *J. Neurosci.* 31:1461–1470. https://doi.org/10.1523/JNEUROSCI.3805-10.2011

Narayanaswamy, N., K. Chakraborty, A. Saminathan, E. Zeichner, K. Leung, J. Devany, and Y. Krishnan. 2019. A pH-correctable, DNA-based fluorescent reporter for organellar calcium. *Nat. Methods*. 16:95–102. https://doi.org/10.1038/s41592-018-0232-7

Navarro, M.X., N.C. Gerstner, S.M. Lipman, G.E. Dolgonos, and E.W. Miller. 2024. Improved sensitivity in a modified berkeley red sensor of transmembrane potential. *ACS Chem. Biol.* 19:2214–2219. https://doi.org/10.1021/acschembio.4c00442

Payandeh, J., and D.L. Minor. 2015. Bacterial voltage-gated sodium channels (BacNa(V)s) from the soil, sea, and salt lakes enlighten molecular mechanisms of electrical signaling and pharmacology in the brain and heart. *J. Mol. Biol.* 427:3–30. https://doi.org/10.1016/j.jmb.2014.08.010

Pinto, L.H., L.J. Holsinger, and R.A. Lamb. 1992. Influenza virus M2 protein has ion channel activity. *Cell*. 69:517–528. https://doi.org/10.1016/0092-8674(92)90452-I

Radchenko, M.V., K. Tanaka, R. Waditee, S. Oshimi, Y. Matsuzaki, M. Fukuhara, H. Kobayashi, T. Takabe, and T. Nakamura. 2006. Potassium/proton antiport system of *Escherichia coli*. *J. Biol. Chem.* 281:19822–19829. https://doi.org/10.1074/jbc.M600333200

Rahamimoff, R., S.A. DeRiemer, B. Sakmann, H. Stadler, and N. Yakir. 1988. Ion channels in synaptic vesicles from Torpedo electric organ. *Proc. Natl. Acad. Sci. USA*. 85:5310–5314. https://doi.org/10.1073/pnas.85.14.5310

Sabatini, B.L., and K. Svoboda. 2000. Analysis of calcium channels in single spines using optical fluctuation analysis. *Nature*. 408:589–593. https://doi.org/10.1038/35046076

Saha, S., V. Prakash, S. Halder, K. Chakraborty, and Y. Krishnan. 2015. A pH-independent DNA nanodevice for quantifying chloride transport in organelles of living cells. *Nat. Nanotechnology*. 10:645–651. https://doi.org/10.1038/nnano.2015.130

Salzer, J.L. 1997. Clustering sodium channels at the node of ranvier: Close encounters of the axon-glia kind. *Neuron*. 18:843–846. https://doi.org/10.1016/S0896-6273(00)80323-2

Saminathan, A., J. Devany, A.T. Veetil, B. Suresh, K.S. Pillai, M. Schwake, and Y. Krishnan. 2021. A DNA-based voltmeter for organelles. *Nat. Nanotechnol.* 16:96–103. https://doi.org/10.1038/s41565-020-00784-1

Schmandt, N.T., and R.F. Galán. 2012. Stochastic-shielding approximation of Markov chains and its application to efficiently simulate random ion-channel gating. *Phys. Rev. Lett.* 109:118101. https://doi.org/10.1103/PhysRevLett.109.118101

Schmid, G., I. Goychuk, and P. Hänggi. 2003. Channel noise and synchronization in excitable membranes. *Physica A Stat. Mech. Appl.* 325:165–175. https://doi.org/10.1016/S0378-4371(03)00195-X

Scott, C.C., and J. Gruenberg. 2011. Ion flux and the function of endosomes and lysosomes: pH is just the start. *BioEssays*. 33:103–110. https://doi.org/10.1002/bies.201000108

Sepehri Rad, M., L.B. Cohen, O. Braubach, and B.J. Baker. 2018. Monitoring voltage fluctuations of intracellular membranes. *Sci. Rep.* 8:6911. https://doi.org/10.1038/s41598-018-25083-7

Sherman, A., and J. Rinzel. 1991. Model for synchronization of pancreatic beta-cells by gap junction coupling. *Biophys. J.* 59:547–559. https://doi.org/10.1016/S0006-3495(91)82271-8

Sherman, A., J. Rinzel, and J. Keizer. 1988. Emergence of organized bursting in clusters of pancreatic beta-cells by channel sharing. *Biophys. J.* 54:411–425. https://doi.org/10.1016/S0006-3495(88)82975-8

Singh, A., F.V. Marcoline, S. Veshaguri, A.W. Kao, M. Bruchez, J.A. Mindell, D. Stamou, and M. Grabe. 2019. Protons in small spaces: Discrete simulations of vesicle acidification. *PLoS Comput. Biol.* 15:e1007539. https://doi.org/10.1371/journal.pcbi.1007539

Skaugen, E., and L. Walløe. 1979. Firing behaviour in a stochastic nerve membrane model based upon the Hodgkin-Huxley equations. *Acta Physiol. Scand.* 107:343–363. https://doi.org/10.1111/j.1748-1716.1979.tb06486.x

Somjen, G.G. 2001. Mechanisms of spreading depression and Hypoxic spreading depression-like depolarization. *Physiol. Rev.* 81:1065–1096. https://doi.org/10.1152/physrev.2001.81.3.1065

Sorgato, M.C., B.U. Keller, and W. Stühmer. 1987. Patch-clamping of the inner mitochondrial membrane reveals a voltage-dependent ion channel. *Nature*. 330:498–500. https://doi.org/10.1038/330498a0

Sze, C., and Y.-J. Tan. 2015. Viral membrane channels: Role and function in the virus life cycle. *Viruses*. 7:3261–3284. https://doi.org/10.3390/v7062771

Takamori, S., M. Holt, K. Stenius, E.A. Lemke, M. Grønborg, D. Riedel, H. Urlaub, S. Schenck, B. Brügger, P. Ringler, et al. 2006. Molecular anatomy of a trafficking organelle. *Cell*. 127:831–846. https://doi.org/10.1016/j.cell.2006.10.030

Tian, H., H.C. Davis, J.D. Wong-Campos, P. Park, L.Z. Fan, B. Gmeiner, S. Begum, C.A. Werley, G.B. Borja, H. Upadhyay, et al. 2023. Video-based pooled screening yields improved far-red genetically encoded voltage indicators. *Nat. Methods*. 20:1082–1094. https://doi.org/10.1038/s41592-022-01743-5

Upmanyu, N., J. Jin, H.v. d. Emde, M. Ganzella, L. Bösche, V.N. Malviya, E. Zhuleku, A.Z. Politi, M. Ninov, I. Silbern, et al. 2022. Colocalization of different neurotransmitter transporters on synaptic vesicles is sparse except for VGLUT1 and ZnT3. *Neuron*. 110:1483–1497.e7. https://doi.org/10.1016/j.neuron.2022.02.008

Van Dyke, R.W., and J.D. Belcher. 1994. Acidification of three types of liver endocytic vesicles: Similarities and differences. *Am. J. Physiol.* 266:C81–C94. https://doi.org/10.1152/ajpcell.1994.266.1.C81

Wang, W., X. Zhang, Q. Gao, M. Lawas, L. Yu, X. Cheng, M. Gu, N. Sahoo, X. Li, P. Li, et al. 2017. A voltage-dependent K+ channel in the lysosome is required for refilling lysosomal Ca2+ stores. *J. Cell Biol.* 216:1715–1730. https://doi.org/10.1083/jcb.201612123

White, J.A., R. Klink, A. Alonso, and A.R. Kay. 1998. Noise from voltage-gated ion channels may influence neuronal dynamics in the entorhinal cortex. *J. Neurophysiol.* 80:262–269. https://doi.org/10.1152/jn.1998.80.1.262

White, J.A., J.T. Rubinstein, and A.R. Kay. 2000. Channel noise in neurons. *Trends Neurosci.* 23:131–137. https://doi.org/10.1016/S0166-2236(99)01521-0

Xu, H., E. Martinoia, and I. Szabo. 2015. Organellar channels and transporters. *Cell Calcium*. 58:1–10. https://doi.org/10.1016/j.ceca.2015.02.006

Yan, P., C.D. Acker, V. Biasci, G. Judge, A. Monroe, L. Sacconi, and L.M. Loew. 2023. Near-infrared voltage-sensitive dyes based on chromene donor. *Proc. Natl. Acad. Sci. USA*. 120:e2305093120. https://doi.org/10.1073/pnas.2305093120

Zeng, S., Y. Tang, and P. Jung. 2007. Spiking synchronization of ion channel clusters on an axon. *Phys. Rev. E Stat Nonlin. Soft. Matter Phys.* 76:011905. https://doi.org/10.1103/PhysRevE.76.011905

Zou, J., K. Mitra, P. Anees, D. Oettinger, J.R. Ramirez, A.T. Veetil, P.D. Gupta, R. Rao, J.J. Smith, P. Kratsios, and Y. Krishnan. 2024. A DNA nanodevice for mapping sodium at single-organelle resolution. *Nat. Biotechnol.* 42:1075–1083. https://doi.org/10.1038/s41587-023-01950-1

Supplemental material

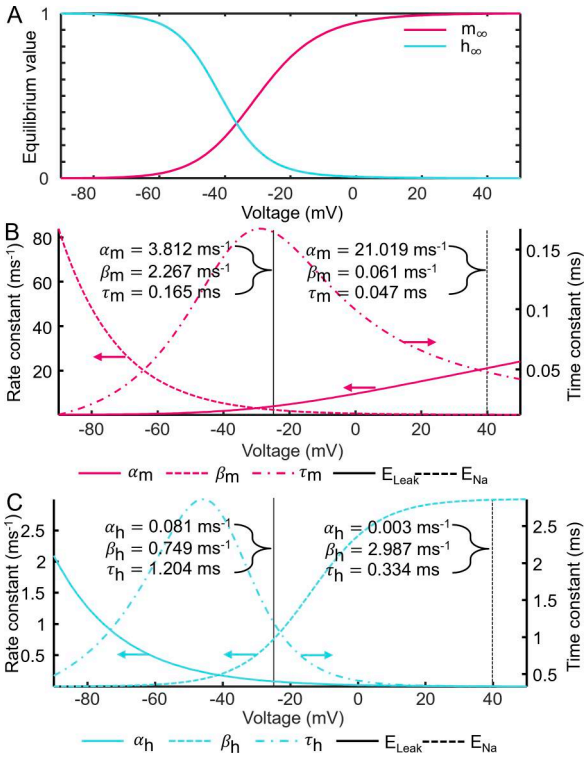

Figure S1. **Na_V model. (A)** Steady-state activation (pink) and inactivation (cyan). **(B)** Voltage-dependent kinetic parameters of the activation (m) gate. Activation rate, α_m (solid); deactivation rate, β_m (dash); time constant τ_m (dash dot). Vertical lines indicate parameter values at the leak reversal (E_{Leak}, solid black line) used in Fig. 2, B–E, and the Na^+ reversal potential (E_{Na}, dashed black line). **(C)** Same as B, for the inactivation (h) gate.

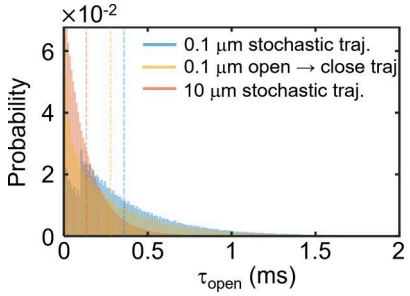

Figure S2. **Time-dependent open-state lifetime in single-channel Na_V vesicles.** Open-state dwell time histograms for spontaneous gating trajectories of single Na_V's in vesicles of radius $r = 0.1\,\mu m$ (blue) and $r = 10\,\mu m$ (orange); simulations 5,000 s. Leak reversal potential, $E_{Leak} = -25$ mV. Shown for comparison are the open-state lifetimes of Na_V in single-channel $r = 0.1\,\mu m$ vesicles were the Na_V is initialized in the open state at $V_m = E_{Leak}$ (yellow); 2×10^5 independent trials. Dashed vertical lines indicate the distribution means; $r = 0.1\,\mu m$ stochastic trajectory $\langle\tau_{open}\rangle = 0.36 \pm 0.33$ ms (blue); $r = 10\,\mu m$ stochastic trajectory $\langle\tau_{open}\rangle = 0.13 \pm 0.13$ ms (orange); and $r = 0.1\,\mu m$ open → closed lifetime $\langle\tau_{open}\rangle = 0.28 \pm 0.31$ ms (yellow); (mean ± SD).

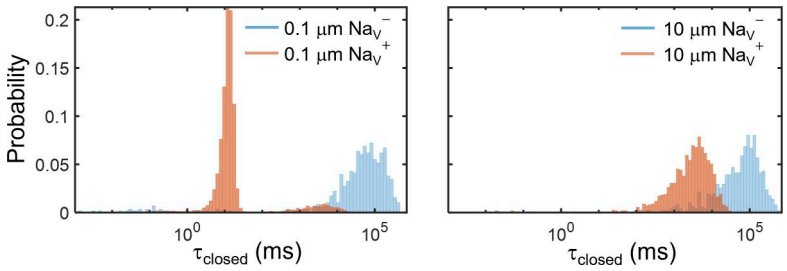

Figure S3. **Nanoscale vesicles support distinct patterns of channel gating.** Closed state dwell-time histograms of spontaneous channel gating in single Na_V vesicles of radii (left) $r = 0.1\,\mu m$ and (right) $r = 10\,\mu m$. HH-type Na_V gating parameters were adjusted to generate a model with substantial window current (denoted by Na_V^+, orange) and a model with negligible window (Na_V^-, blue). Na_V^+ simulations: 5,000 s; Na_V^- results are aggregated from five independent trials of 5,000-s simulations. $E_{leak} = -60$ mV. Modified gating model parameters are described in Supplemental text Note S1.

Provided online are Table S1 and Table S2. Table S1 shows electrophysiological parameters and initial conditions of the HH neuron-type vesicle model. Table S2 shows electrophysiological parameters and initial conditions of the endosome model.

Note S1

Markov model of Na_V and K_V gating. Diagram adapted from Destexhe and Huguenard (2009). I, inactivated; C, closed; O, open.

Na_V

Scheme 1.

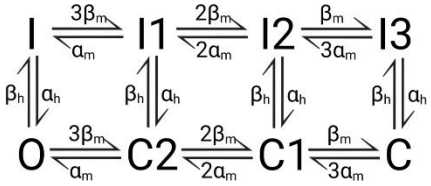

K_V

Scheme 2.

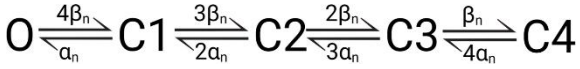

Transition rate functions for default Na_V model, adapted from Hübel et al. (2014), where all times are measured in milliseconds and all voltages in millivolts:

$$\alpha_m = \frac{0.1(V + 30 + S_m)}{1 - \exp\left(-\frac{(V+30+S_m)}{10A_m}\right)}$$

$$\beta_m = 4\exp\left(-\frac{(V + 55 + S_m)}{18A_m}\right)$$

$$\alpha_h = 0.07\exp\left(-\frac{(V + 44 + S_h)}{20A_h}\right)$$

$$\beta_h = \frac{1}{1 + \exp\left(-\frac{(V+14+S_h)}{10A_h}\right)}$$

$$\alpha_n = \frac{0.01(V + 34)}{1 - \exp\left(\frac{-(V+34)}{10}\right)}$$

$$\beta_n = 0.125\exp\left(-\frac{(V + 44)}{80}\right)$$

Default Na_V contains moderate window currents: $S_m = S_h = 0$; $A_m = A_h = 1$.

Na_V with large window currents (Na_V^+): S_m = 10; S_h = −10; A_m = 0.55; A_h = 0.55.
Na_V with small window currents (Na_V^-): S_m = −10; S_h = 19; A_m = 0.95; A_h = 1.

Note S2

$Na_V1.5$ state diagram and transition rate functions from Balbi et al. (2017). The unified model developed by Balbi et al. accounts for $Na_V1.1$–1.9 dynamics using fewer channel states than the Markov model of HH-type Na_V (see Note S1) and isoform-specific gating rates.

Scheme 3.

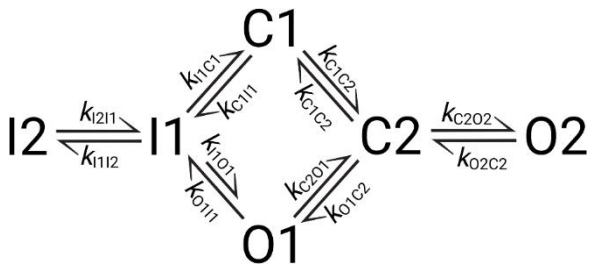

I, inactivated; C, closed; O, open. All times are measured in milliseconds and all voltages in millivolts:

$$k_{C1C2} = \frac{10}{1 + e^{\frac{V-(-13)}{-10}}}$$

$$k_{C2C1} = \frac{1}{1 + e^{\frac{V-(-43)}{8}}} + \frac{10}{1 + e^{\frac{V-(-13)}{-10}}}$$

$$k_{C2O1} = \frac{10}{1 + e^{\frac{V-(-23)}{-10}}}$$

$$k_{O1C2} = \frac{1}{1 + e^{\frac{V-(-53)}{8}}} + \frac{10}{1 + e^{\frac{V-(-23)}{-10}}}$$

$$k_{C2O2} = \frac{0.05}{1 + e^{\frac{V-(-10)}{-10}}}$$

$$k_{O2C2} = \frac{2}{1 + e^{\frac{V-(-50)}{10}}} + \frac{0.08}{1 + e^{\frac{V-(-20)}{-10}}}$$

$$k_{O1I1} = \frac{7}{1 + e^{\frac{V-(-44)}{13}}} + \frac{10}{1 + e^{\frac{V-(-19)}{-13}}}$$

$$k_{I1O1} = \frac{1 \times 10^{-5}}{1 + e^{\frac{V-(-20)}{10}}}$$

$$k_{I1C1} = \frac{0.19}{1 + e^{\frac{V-(-110)}{7}}}$$

$$k_{C1I1} = \frac{0.016}{1 + e^{\frac{V-(-92)}{-6}}}$$

$$k_{I1I2} = \frac{2.2 \times 10^{-4}}{1 + e^{\frac{V-(-50)}{-5}}}$$

$$k_{I2I1} = \frac{1.8 \times 10^{-3}}{1 + e^{\frac{V-(-90)}{30}}}$$